Marine Geology 455 (2023) 106954

Contents lists available at ScienceDirect

Marine Geology

journal homepage: www.elsevier.com/locate/margo

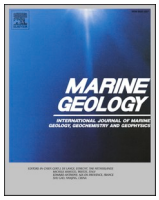

Pyrites in a salt marsh-ria system: Quantification, morphology, and mobilization

X.L. Otero [a,b,*], P. Guevara [a,c], M. Sánchez [d], I. López [c], H.M. Queiroz [e], A. Ferreira [e], T.O. Ferreira [e], G.N. Nóbrega [f], R. Carballo [d]

[a] CRETUS, Cross-disciplinary Research in Environmental Technologies, Departamento de Edafoloxía e Química Agrícola, Facultade de Bioloxía, Universidade de Santiago de Compostela, Spain
[b] REBUSC Rede de Estacións Biolóxicas da Universidade de Santiago de Compostela, Estación de Bioloxia Mariña A Graña, Ferrol, Spain
[c] Departamento de Ciencias de la Tierra y la Construcción, Universidad de las Fuerzas Armadas ESPE, Av. General Rumiñahui s/n, P.O. Box 171-5-231B, Sangolquí, Ecuador
[d] Área de Ingeniería Hidráulica, EPSE, Universidade de Santiago de Compostela, Lugo, Spain
[e] Luiz de Queiroz College of Agriculture, Soil Science Department University of São Paulo (ESALQ-USP), Av. Pádua Dias 11, CEP 13418-900, Piracicaba, São Paulo, Brazil
[f] Departamento de Geoquímica, Instituto de Química, Universidade Federal Fluminense, Brazil

ARTICLE INFO

Editor: Dr. Adina Paytan

Keywords:
Salt marsh
Soil
Sediment
Ría
Pyrite
Framboids

ABSTRACT

Galician Rias are among the most productive ecosystems in the world. Consequently, the soils of their salt marshes and sediments of the intertidal flats show high organic matter contents, reactive Fe, and sulfate, which promote pyrite synthesis and accumulation, using sulfate for organic matter decomposition. This work studies the morphological variability and concentration of pyrites (individual crystals and framboids) in different geochemical environments found in the Ria de Ortigueira (salt marsh soils and bottom sediments in the inner, middle, and outer section), addressing their dynamics in the marsh-ria system in relation to the hydrodynamic characteristics defined by tides and river discharges. Framboidal pyrites were the dominant morphology in marsh soils and sediments in the middle and inner sections of the Ria, while isolated crystals dominated its outer section. The results showed that lower marsh soils (colonized by *Spartina*) are the most favorable environment for pyrite synthesis, showing high pyritic Fe concentrations and high degrees of pyritization, largely exceeding the values observed in sediments from Galician Rias and from most sedimentary environments worldwide. However, the amount of framboidal pyrites present in the lower marsh (SPE: 4–5 $\times$ 10^4 framboids) was clearly lower than in bottom sediments of the inner and middle part of the Ria de Ortigueira (~2–7 $\times$ 10^6 framboids), mainly due to the fact that pyrites were found to form large framboids in lower salt marsh soils. Thus, the amount of framboidal pyrites does not seem to be a good indicator of redox conditions in modern marine sediments. Pyrite crystals found in the sediments of the Ria showed poorly defined vertices and facets, indicating their degradation and suggesting that a significant amount of the pyrites found in the middle and inner sections derive from marsh collapse. Finally, the output of framboidal pyrites towards the outer Ria de Ortigueira reflects the low intensity of residual flows in this Ria. Therefore, the pyrites observed in the outer section consisted only of isolated crystals, presumably formed in situ under low sulfate-reducing activity conditions.

1. Introduction

Salt marshes and *Rias* are among the most productive ecosystems on Earth (Margalef, 1952; Odum and Odum, 1981). Both ecosystems show high primary productivity, which results in high organic matter contents in their soils and sediments (Howarth and Teal, 1979; Otero and Macías, 2002, 2003, 2010), but also act as sinks receiving significant contributions of inorganic materials (e.g., clay and silt) and dissolved elements from rivers and wastewater discharges (Filgueiras and Prego, 2007).

The high organic matter contents in its soils and sediments are

* Corresponding author at: CRETUS, Cross-disciplinary Research in Environmental Technologies, Departamento de Edafoloxía e Química Agrícola, Facultade de Bioloxía, Universidade de Santiago de Compostela, Spain.
E-mail address: xl.otero@usc.es (X.L. Otero).

https://doi.org/10.1016/j.margeo.2022.106954
Received 24 June 2022; Received in revised form 16 November 2022; Accepted 22 November 2022
Available online 24 November 2022

related to the redox conditions imposed by the tidal variations and seasonal patterns in sea currents (Kirwan and Mudd, 2012). Under such conditions, anaerobic pathways of organic matter decomposition may prevail and promote pyrite formation and accumulation (Oenema, 1990; Souza et al., 2009). Several studies have pointed out that organic matter in salt marsh soils and sediments is mainly oxidized by reducing Fe oxyhydroxides and sulfate (Wiebe et al., 1981; Howarth, 1984, Canfield et al., 1992). The coupling of these two anaerobic pathways increases the concentration of Fe^{2+} and reduced S forms (i.e., HS^-, polysulfides) in interstitial waters and, ultimately, promotes pyrite (FeS_2) formation (Canfield et al., 1992; Otero and Macías, 2010). Under anoxic conditions, pyrite is considered the most stable final product of sulfate reduction (Howarth, 1984), but is also responsible for relevant ecological services, such as trace metal retention (Otero and Macías, 2003). In fact, pyrites significantly control the biogeochemistry of several elements within marine and intertidal sedimentary environments (Howarth, 1984).

In strongly reduced environments, pyrite is formed with mackinawite (FeS_{mk}) as a precursor, and H_2S acts as an oxidant in a kinetically fast reaction that can take place within days (Reaction 1; Rickard, 1970; Lan and Butler, 2014).

$$FeS_{(mk)} + H_2S \rightarrow FeS_2 + H_2 \quad \text{Reaction (1)}$$

Conversely, in environments with alternating redox conditions (e.g., salt marsh soils in higher physiographic positions), the diffusion of oxygen into the substrate promotes the precipitation of poorly crystalline Fe oxyhydroxides (e.g., lepidocrocite) and the formation of polysulfides (S_5^{-2}) due to the partial oxidation of H_2S (Reaction 2). Under these oscillating redox conditions, pyrite is formed by two different pathways: (i) through FeS as an intermediate product (Reactions 4, 5), with slower kinetics (i.e., within years; Luther III, 1991; Rickard, 2012; Peiffer and Behrends, 2015), and (ii) by the direct precipitation from interstitial water occurring within days (Reaction 5; Howarth and Teal, 1979; Giblin and Howarth, 1984).

$$8FeOOH + 5H_2S \rightarrow 8Fe^{2+} + S_5^{2-} + 2H_2O + 14OH^- \quad \text{Reaction (2)}$$

$$Fe^{2+} + SH^- \rightarrow FeS + H^+ \quad \text{Reaction (3)}$$

$$4FeS + S_5^{2-} + 2H^+ \rightarrow 4FeS_2 + H_2S \quad \text{Reaction (4)}$$

$$Fe^{2+} + S_5^{2-} + HS^- \rightarrow FeS_2 + S_4^{2-} + H^+ \quad \text{Reaction (5)}$$

Although pyrite is a major sink for Fe and other trace elements (Berner, 1967; Huerta-Díaz and Morse, 1992; Otero and Macías, 2003), redox conditions may considerably affect its role as a metal scavenger. For example, pyrite microcrystals are stable under anoxic conditions and may experience regrowth once buried (Rickard, 2012) whereas, under oxic and near neutral to alkaline conditions (e.g., seawater), pyrite can be oxidized within short periods (i.e., days or weeks; Aller, 1980; Morse, 1991). In this context, the influence of sea currents, catastrophic events such as storms (Scheffer et al., 2001), and coastal erosion events (Bertness et al., 2005; Ruggiero, 2012; Taherkhani et al., 2020) can transport, redistribute, and oxidize pyrite crystals releasing the associated elements into seawater (Morse, 1991; Otero et al., 2005). Some of these elements are essential limiting nutrients for marine primary productivity (e.g., Cu, Co, Fe), while others are potentially toxic (e.g., As, Hg, Cd, Pb) to several living organisms.

Thus, combining chemical extractions for Fe partitioning, electron microscopy for pyrite morphological analysis, and numerical hydrodynamic modeling, this study aims to improve our understanding of the connections between salt marshes and the surrounding sedimentary environments and their role in nutrient and pollutant transfer from the continent to the ocean.

2. Material and methods

2.1. Description of the study area and sampling procedures

The Ria de Ortigueira and the studied salt marshes are located in the NW Iberian Peninsula (latitude UTM: 4841094 N, longitude UTM: 593782 E, Zone 29 T, Fig. 1), showing a mesotidal regime, with a maximum range of 4.5 m. In recent years, the progressive collapse of salt marsh channels and edges has been observed, the resulting material falling directly into the inner and middle sections of the Ria or being transported from the channels into the Ria (Fig. 1). The freshwater input is small, with a mean discharge of approximately 8 $m^3\ s^{-1}$ during the winter and 3 $m^3\ s^{-1}$ in the summer.

Two soil cores were drilled from the Esteiro salt marsh: the first located in a lower physiographic position and dominated by *Spartina maritima* (cordgrass), and the second located a drainage channel. Next, one soil core was drilled in the Mera salt marsh, located in a higher physiographic position and covered by *Spartina maritima*, and, finally, one soil core was drilled in the Ladrido salt marsh occupied by *Juncus maritimus* (sea rush), also in a higher physiographic position (Fig. 1). Cores were collected using 50-cm-long polyvinyl chloride tubes (PVC) with an internal diameter of 11 cm. After sampling, soil cores were transported to the laboratory in a vertical position and under refrigeration (~4 °C). In the laboratory, samples were removed from the tubes and sectioned into 3-cm-long sections for the upper 15 cm and 5-cm-long sections for the deeper portion to obtain subsamples for analysis. The following salt marsh subsamples were then selected for analysis: Esteiro salt marsh dominated by *Spartina maritima*, 0–3 cm layer (referenced as SPE 0–3 cm) and 15–35 cm layer (SPE2 15–35 cm); drainage channel of the Esteiro salt marsh, 0–15 cm layer (0–15 CE cm); Mera salt marsh dominated by *Spartina*, 0–3 cm (SPM1 0–3 cm) and 15–45 cm layers (SPM2 15–45 cm); and Ladrido salt marsh occupied by *Juncus maritimus*, 0–3 cm (JL1 0–3 cm) and 15–35 cm soil layers (JL2 15–35 cm).

Additionally, surface samples (0–10 cm) from the bottom sediment of the Ria de Ortigueira were collected using a gravity corer ($n = 117$; Fig. 1) along the central channel, which was divided into three sections according to hydrodynamic conditions: a) inner section (IS), spanning from the mouth of the River Mera to Ortigueira county, b) middle section (MS), from the Esteiro salt marsh to the Caldeira inlet, and c) outer section (OS), from the Ladrido salt marsh to the open ocean shore (Fig. 1; Guevara et al., 2021). Samples were stored in plastic ziplock bags and transported to the laboratory in the dark at a temperature of ~4 °C. To study pyrite size and morphology, seven samples from the IS, five from the MS, and seven from the OS were analyzed. Subsamples of each soil and sediment sample were frozen at −20 °C for Fe partitioning and pyrite analysis, while the remaining samples were air dried at 45 °C.

2.2. Analytical methods

2.2.1. Characterization of hydrodynamics of the Ria de Ortigueira

The hydrodynamics of the Ria was computed through high-resolution numerical modeling using the Delft3D-FLOW model. This model solves the 3D Navier-Stokes and transport equations reading:

$$\frac{\partial u}{\partial x} + \frac{\partial v}{\partial y} + \frac{\partial w}{\partial z} = S \quad (1)$$

$$\frac{Du}{Dt} = fv - g\frac{\partial \zeta}{\partial x} - \frac{g}{\rho_0}\int_{z'=z}^{z'=\zeta}\frac{\partial \rho}{\partial x}dz' + \upsilon_h\left(\frac{\partial^2 u}{\partial x^2} + \frac{\partial^2 u}{\partial y^2}\right) + \upsilon_v\left(\frac{\partial^2 u}{\partial z^2}\right)\frac{Dv}{Dt} = -fu - g\frac{\partial \zeta}{\partial y} - \frac{g}{\rho_0}\int_{z'=z}^{z'=\zeta}\frac{\partial \rho}{\partial y}dz' + \upsilon_h\left(\frac{\partial^2 v}{\partial x^2} + \frac{\partial^2 v}{\partial y^2}\right) + \upsilon_v\left(\frac{\partial^2 v}{\partial z^2}\right) \quad (2)$$

$$\frac{\partial p}{\partial z} = -\rho g \quad (3)$$

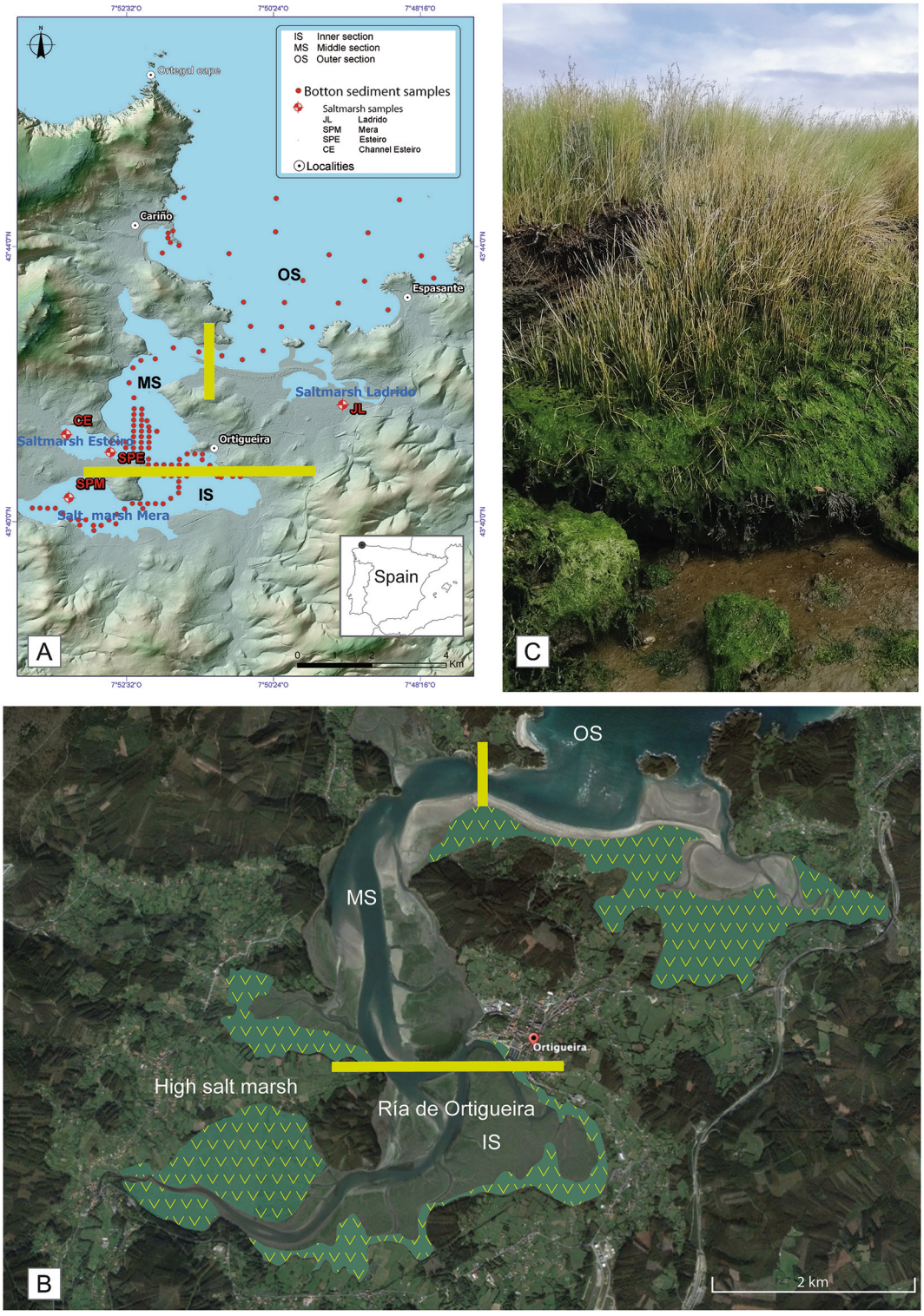

Fig. 1. A) Study area and sampling sites (salt marshes: red and white circles; bottom sediments: red circles). The Ria de Ortigueira sectors (IS - inner section; MS - middle section, and OS - outer section) were defined based on their hydrodynamic characteristics. B) Distribution of salt marshes systems in the ria de Ortigueira. C) Photograph showing the progressive collapse of the salt marsh edges. (For interpretation of the references to colour in this figure legend, the reader is referred to the web version of this article.)

$$\frac{Dc}{Dt} = D_h\left(\frac{\partial^2 c}{\partial x^2} + \frac{\partial^2 c}{\partial y^2}\right) + D_v\frac{\partial^2 c}{\partial z^2} - \lambda_d c + R_s \tag{4}$$

Eq. 1 represents the mass conservation for an incompressible fluid; Eq. 2 stands for momentum conservation in the x and y directions; Eq. 3 represents momentum conservation in the z-direction, which, under shallow water conditions, turns into the hydrostatic pressure equation; finally, Eq. 4 represents the transport equation, which, in the present application, is solved for salinity and temperature conditions. In the mass conservation equation, u, v, and w express the velocity components in the x, y, and z directions, respectively, and S is the source term. In

addition, in the momentum conservation equations, t is time, g is gravity acceleration, f is the Coriolis parameter, ζ is the elevation of the sea surface for $z = 0$, υ_h and υ_v are the horizontal and vertical turbulent eddy viscosity, respectively, ρ_h and ρ_0 are the density and the reference density of ocean water, respectively, and p is pressure. Finally, in the transport equation, c is a constituent representing salinity or temperature, D_h and D_v are the horizontal and vertical turbulent eddy diffusivity, respectively, λ_d is the decay process of the first order, and C_s is the source term. More information about model implementation can be found in Sánchez et al. (2014).

As stated, the main objective of implementing the numerical model was to model the hydrodynamic capacity of the Ria to transport pyrite and to alter its distribution within the Ria system. To this end, the transient and residual flows were computed during a typical winter period, which is considered to have higher sediment transport capacity (due to the greater river discharge compared with the summer season). Furthermore, the residual flows were computed considering the action of tidal constituent M_2 (i.e., the largest lunar constituent) and winter river discharges. In particular, the model was applied during a spring-neap tidal cycle, using the following as boundary conditions: (i) main tidal constituents, (ii) oceanic characteristics (salinity and temperature), and (iii) river discharge in the inner Ria, considering the average values during the period of interest ($Q = 8\ m^3 s^{-1}$).

2.2.2. Analysis of salt marsh soils and sediments

During sampling, redox potential (Eh) values were measured using an oxidation-reduction potential platinum electrode with final readings corrected by adding the potential value (+244 mV) of a calomel reference electrode. The pH values were measured using a Crisol micropH 2000 pHmeter with a glass electrode previously calibrated with standard solutions (pH 4.0 and 7.0). Total organic carbon (TOC) contents were determined using a Leco TruSpec CHN device by calculating the difference between total C and inorganic C; the latter was determined on samples after removing organic C by calcination at 450 °C for 4 h (Cambardella et al., 2001). Total sulfur (S_{total}) was determined using a Leco SC-144DR analyzer. Finally, particle size distribution was determined by the pipette method (Gee and Bauder, 1986) after the removal of soil organic matter using 6% NaClO at pH 8.0 (Mikutta et al., 2005). All analyses were carried out on samples from the 117 sampling sites for bottom sediments in the channel of the Ria (0–10 cm) and on four salt marsh soil cores.

A sequential extraction procedure was performed to obtain pyritic (Fe_{py}) and reactive Fe ($Fe_{reactive}$). $Fe_{reactive}$ was extracted using 20 ml of a 0.25 M sodium citrate +0.11 M $NaHCO_3$ solution and 3 g sodium dithionite (Canfield et al., 1992), whereas Fe_{py} was extracted using 10 ml of concentrated HNO_3 after removing Fe silicate-associated (by treating with 10 M HF and shaking for 16 h) and organic matter-associated Fe (by treating with concentrated H_2SO_4; see Huerta-Díaz and Morse, 1992). Both fractions ($Fe_{reactive}$ and Fe_{py}) were analyzed by atomic absorption spectroscopy. The degree of Fe pyritization (DOP), which allows for the comparison of pyritization under different Fe contents, was calculated according to Berner (1970; Equation 5).

$$DOP\ (\%) = \frac{(Fe_{py})}{(Fe_{py} + Fe_{reactive})} x\ 100 \tag{5}$$

2.2.3. Pyrite morphology and size

Pyrites were concentrated from sediment samples and soil subsamples (i.e., SPE1 0–3 cm, SPM1 0–3 cm, JL1 0–3 cm, and JL2 15–35 cm) by the bromoform decanting method ($\rho = 2.89\ g\ cm^{-3}$, Wilkin et al., 1996'). For this, 9 g of freeze-dried samples were weighed, carefully disaggregated with a mortar, and moved to a decantation funnel; after shaking, they were left to decant overnight. The dense fraction deposited at the bottom of the decantation tube was washed with acetone and placed in an aluminum tray. Pyrite size and morphology were determined by scanning electron microscopy (SEM) (FESEM Zeiss Ultra Plus with EDX-Image) at a resolution of 0.8 nm and an accelerating voltage of 30 kV.

The pyrites were divided into five categories: 1) individual framboids, 2) framboid clusters, 3) isolated crystals, 4) framboidal pyrites within diatom frustules, and 5) framboidal pyrites within plant tissues. Framboid sizes were assessed based on size distribution histograms using geometric parameters and log-normal histograms (Limpert and Stahe, 2011; Rickard, 2019b). Statistical parameters $\bar{x}$ = arithmetic means and σ = standard deviation were subjected to geometric transformation using the parameter (ω), which allows for arithmetic transformation into geometric parameters. It is expressed as $\omega = 1 + (\sigma/\bar{x})^2$ (Limpert and Stahe, 2011; Rickard, 2019b), which allows calculating the geometric mean ($\bar{x}^* = \bar{x}/\sqrt{\omega}$) and the geometric standard deviation $\sigma^* = \exp.(\sqrt{\ln(\omega)})$ (for further details, see Rickard, 2019a).

2.2.4. Distribution of framboidal pyrites in the salt marsh-ria system

This calculation considered the volume of each sphere, the mass corresponding to that volume, and pyrite contents obtained from Fe_{py} content, assuming that all Fe_{py} was found in the framboidal form. Eqs. 6–8 were used for this calculation, additionally assuming that framboids were solid spheres without interstitial spaces; their diameter was assumed to be the previously calculated geometric diameter (Limpert and Stahe, 2011; Rickard, 2019b):

$$\text{Sphere volume}: V\ (cm^3) = \frac{4}{3}\pi\left(\frac{\bar{x}^*}{2}\right)^3 \tag{6}$$

$$\text{Mass of a pyrite sphere}\ (g): m_P = d_{P^*} V \tag{7}$$

$$\text{No.of framboids}\ (\text{framboids}\ g^{-1}): N_{framboides} = \frac{Fe_{py}{}^* MW_{py}}{m_p} \tag{8}$$

Where:

$\bar{x}^*$: mean geometric diameter of pyrites in each section of the *Ria* or each type of salt marsh, d_p: pyrite density = 5.1 g cm^3; Fe_{py}: mean content of pyritic Fe in each section, and MW_{py}: molecular weight of pyrite = 120 g mol^{-1}.

2.3. Statistical analysis

Descriptive statistics were performed using the Minitab17 software. Frequency histograms for framboidal pyrite sizes were built using a log-normal function (Rickard, 2019b), whereas relationships among variables were established using Spearman correlation tests. Significant differences in the characteristics of pyrite among sites (types of salt marshes or sections of the Ria) or depths (surface/deep) were determined by a one-way ANOVA, followed by a post hoc Holm-Sidack test, or a Mann-Whitney test, using the SigmaPlot 12.0 software. Furthermore, the comparisons among Ria sectors and salt marsh soils were also performed using discriminant analysis (DA), which develops a function that yields optimal discrimination of the Ria sectors (IS, MS, and OS) and salt marsh soils (SPE, SPM, CE, JL). Thus, through DA, the relative contribution of the variables to the separation of the groups can be identified, i.e., the most important variables for the sectors and salt marsh soils (Reimann et al., 2008).

3. Results

3.1. Transient flow dynamics and residual current

The circulation at the IS and MS and the inner section of OS are tide-dominated, evidenced by similar flows throughout the water column (Fig. 2), with slightly lower velocities in the bottom layers, reversed during flood and ebb tides. Concerning the middle and outer sections of OS, the greater depth and width result in a lower tidal circulation and a more significant contribution of river discharges to the local

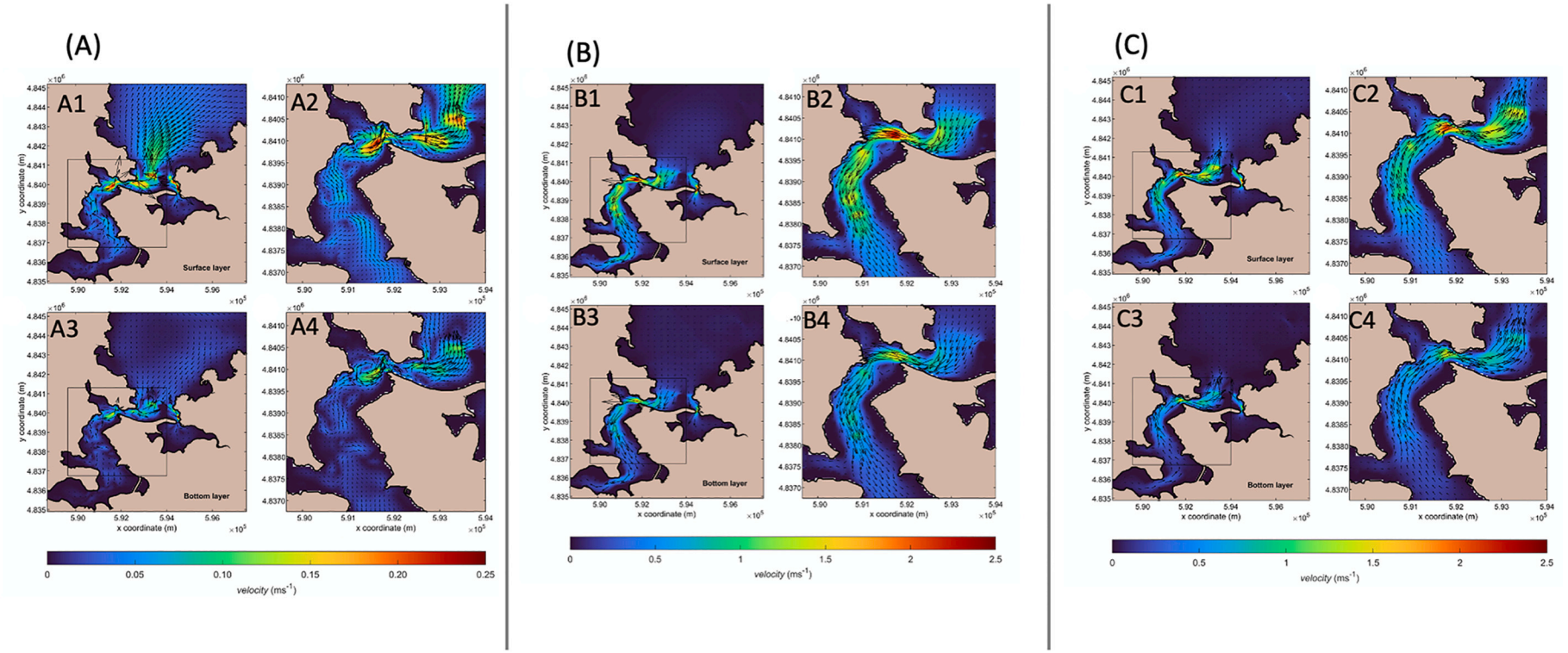

Fig. 2. A) Transient circulation at mid-flood tide in surface (A1 and A2) and bottom (A3 and A4) layers during average spring tides and average winter freshwater discharges. B) Transient circulation at mid-ebb tide in surface (B1 and B2) and bottom (B3 and B4) layers during average spring tides and average winter freshwater discharges. C) M_2 tide-induced residual circulation and freshwater discharge in winter in surface (C1 and C2) and bottom (C3 and C4) layers.

hydrodynamics. However, the existing river discharges cannot significantly alter this area's transient flow, which could also be described as a tide-dominated circulation.

The highest flow velocities are found in MS, mostly ranging from 1.0 to1.5 m s^{-1}, but eventually reaching 2.0 to 2.5 m s^{-1} near its boundaries with OS. In IS, velocity is significantly lower, approximately 0.2 m s^{-1}, with exceptions reaching 0.7 ms^{-1}. Finally, in OS, the flow pattern shows significant variations. In its innermost part, close to MS, velocities are higher (up to 1.5 m s^{-1}) while downstream, at the middle and outer areas, where the depth and width of the Ria increases, velocities decrease to values close to 0.1 m s^{-1}. As a result, intense wind action could significantly influence the hydrodynamics in OS's middle and outer portions.

The residual circulation patterns varied widely throughout the Ria. Vertically homogeneous downstream flows were present in IS, MS, and the inner section of OS (Fig. 2), although with slightly lower velocities in the bottom layers and a 3D flow in the middle and outer portions of OS. The largest magnitudes of residual circulation were found in the same areas as for transient circulation. Transient circulation was concentrated in a limited area corresponding to the outer sections of MS and the inner section of OS, with downstream velocities around 0.20–0.25 m s^{-1} in the surface layer and 0.15 m s^{-1} in the bottom layer.

In this context, to determine the potential for pyrite transport in the different areas, residual flows were computed considering the action of tidal constituent M_2 and winter river discharges (Fig. 2). The overall pattern corresponds to a positive estuarine circulation, evidencing the greater importance of river discharge over the tide for generating net circulation in this area. Finally, concerning IS, residual velocities are weak throughout the water column (~0.01 m s^{-1}), one order of magnitude lower than in MS.

3.2. General characteristics of sediments and soils

Bottom sediments from the three sections of the Ria were dominated by sand (average sand contents ranged from 71 to 93%; Table 1), increasing from the inner to the outer section. Texture in the IS and MS was highly variable, with samples showing fine fractions (i.e., silt and clay) accounting for 90%, whereas other sites showed sand contents higher than 95%.

Table 1
Properties and composition of bottom sediments and salt marsh soils from the Ría de Ortigueira (mean ± SD).

Sample	pH	Eh	Sand	Clay+Silt	TOC	S_{total}
		mV	-			
Bottom sediments						
IS (n = 64)	7.3 ± 0.2	+112 ± 143	71 ± 25	29 ± 25	1.75 ± 1.28	0.54 ± 0.43
MS (n = 28)	7.6 ± 0.1	+314 ± 137	89 ± 25	11 ± 28	0.92 ± 1.42	0.19 ± 0.19
OS (n = 25)	7.4 ± 0.1	+311 ± 134	93 ± 10	7 ± 10.8	0.57 ± 0.50	0.15 ± 0.07
Low salt marsh soils						
SPE1 0–3 cm (n = 1)	6.2	+459	1.8	98.2	6.31	0.48
SPE2 15–35 cm (n = 4)*	6.0 ± 0.2	+35 ± 123	7.1 ± 7.7	92.9 ± 7.7	5.30 ± 1.04	3.06 ± 1.64
Salt marsh channel						
CE (n = 10)	7.1 ± 0.2	+97 ± 114	10.6 ± 1.8	89.4 ± 1.8	1.63 ± 1.02	0.79 ± 0.52
High salt marsh soils						
SPM1 0–3 cm (n = 1)	6.8	-39	2.6	97.4	7.31	1.42
SPM2 15–45 cm (n = 4)*	6.8 ± 0.1	-85 ± 6	3.3 ± 0.9	96.7 ± 0.9	4.62 ± 0.29	1.97 ± 0.48
JL1 0–3 cm (n = 1)	6.3	+456	4.3	95.7	9.73	0.40
JL2 15–35 cm (n = 4)*	6.3 ± 0.1	+159 ± 17	7.4 ± 1.7	92.6 ± 1.7	3.58 ± 1.84	0.16 ± 0.08

Sediment pH ranged from 6.9 to 7.9, and redox conditions ranged from strongly reduced (Eh < +100 mV) to oxic (Eh > +400 mV; Table 1). On average, IS showed significantly lower Eh (compared with MS and OS (Table 1). TOC and S_{total} contents decreased from IS (TOC: 1.75 ± 1.28%; S_{total}:0.54 ± 0.43%) to OS (TOC: 0.57 ± 0.50%; S_{total}:0.15 ± 0.07%; Table 1).

Salt marsh soils showed a finer and more homogeneous grain size composition than sediments, with a dominance of fine fractions (mean values ranging from 89% to 98%; Table 1). The pH values were circumneutral, with the lowest values found in the upper layer of SPE soils (i.e., the lower salt marsh; pH at SPE1 0–3 cm = 6.2; Table 1). SPE soils also showed the highest Eh values (SPE1 0–3 cm: +459 mV), showing a decreasing trend at greater depths (SPE2 15–35 cm, Eh = +35 ± 123 mV; Table 1), indicating an anoxic environment. The remaining soils occupied by cordgrass in the higher salt marsh (SPM) and the channel (CE) showed the dominance of anoxic conditions (average Eh < +100 mV; Table 1), with higher pH values (average: 6.8 ± 0.1 and 7.1 ± 0.2 for SPM and CE, respectively).

TOC was >6% in all salt marsh surface samples (0–3 cm) influenced by the presence of plants, with a marked decrease with depth (TOC in the 15–35 cm depth < 6%) and with the CE samples showing the lowest contents (Table 1). A different behavior was observed for S_{total} contents. In soils colonized by cordgrass (SPE and SPM), S_{total} contents increased with depth, from 0.48% in the upper 0–3 cm to 3.06 ± 1.64% at 15–35 cm in SPE, and from 1.42% to 1.97 ± 0.48% in SPM. Sea rush soils (JL) showed lower S_{total} contents, with lower values at deeper layers (Table 1).

3.3. Geochemical forms of Fe and DOP

The bottom sediments from the Ria showed $Fe_{reactive}$ concentrations 3 to 25-fold higher than those of Fe_{py} in the three sections (Table 2). IS showed the highest $Fe_{reactive}$ (202 ± 56.1 μmol g^{-1}), Fe_{py} (71.9 ± 50 μmol g^{-1}), and DOP (23.8 ± 14.8%) contents, compared with the other sections (Table 2). In MS, $Fe_{reactive}$ and Fe_{py} values were 137 ± 70.4 μmol g^{-1} and 11.3 ± 20.1 μmol g^{-1}, respectively, with a DOP value of 5.6 ± 8.1% (Table 2). In OS, $Fe_{reactive}$ (74.8 ± 28.5 μmol g^{-1}), Fe_{py} (2.4 ± 2.3 μmol g^{-1}), and DOP (2.6 ± 1.6%) were clearly lower (Table 2).

Considering the results observed by the discriminant analysis (DA, Fig. 3), higher Fe_{pyrite} and DOP were highly related to higher S_{total} and TOC contents, which were associated with IS samples but inversely related to Eh and sand. On the other hand, MS and OS were associated with higher Eh and sand contents and lower S_{total}, DOP, TOC, and Fe_{pyrite}. The differentiation between MS and OS zones could be better explained by higher pH values observed at MS (Fig. 3A).

The highest Fe_{py} contents were found in SPM2 15–45 cm, followed by CE, SPE2 15–35 cm, SPM1 0–3 cm, SPE1 0–3 cm, JL1 0–3 cm, and JL2

Table 2
Reactive ($Fe_{reactive}$) and pyrite Fe (Fe_{py}) and degree of Fe pyritization (DOP) in bottom sediments and salt marsh soils from Ria de Ortigueira (mean ± SD).

Sample	$Fe_{reactive}$	Fe_{py}	DOP
	μmol g^{-1}		%
Bottom sediments - Ría			
IS (n = 7)	202 ± 56.1	71.9 ± 50	24 ± 15
MS (n = 5)	137 ± 70.4	11.3 ± 20.1	5.6 ± 8.1
OS (n = 7)	74.8 ± 28.5	2.4 ± 2.3	2.6 ± 1.6
Low salt marsh soils			
SPE 0–3 cm (n = 1)	239	21.1	8.1
SPE 15–35 cm (n = 2)	77.4 ± 37.0	231 ± 27.6	75 ± 11
Salt marsh channel			
CE (n = 3)	73.0 ± 29.0	263 ± 104	76 ± 16
High salt marshes soils			
SPM 0–3 cm (n = 1)	200	81.0	29
SPM2 15–45 cm (n = 2)	64.2 ± 12.7	320 ± 40.3	83 ± 1.0
JL 0–3 cm (n = 1)	253	2.1	0.8
JL 15–35 cm (n = 2)	292 ± 68	1.3 ± 0.2	0.4 ± 0.2

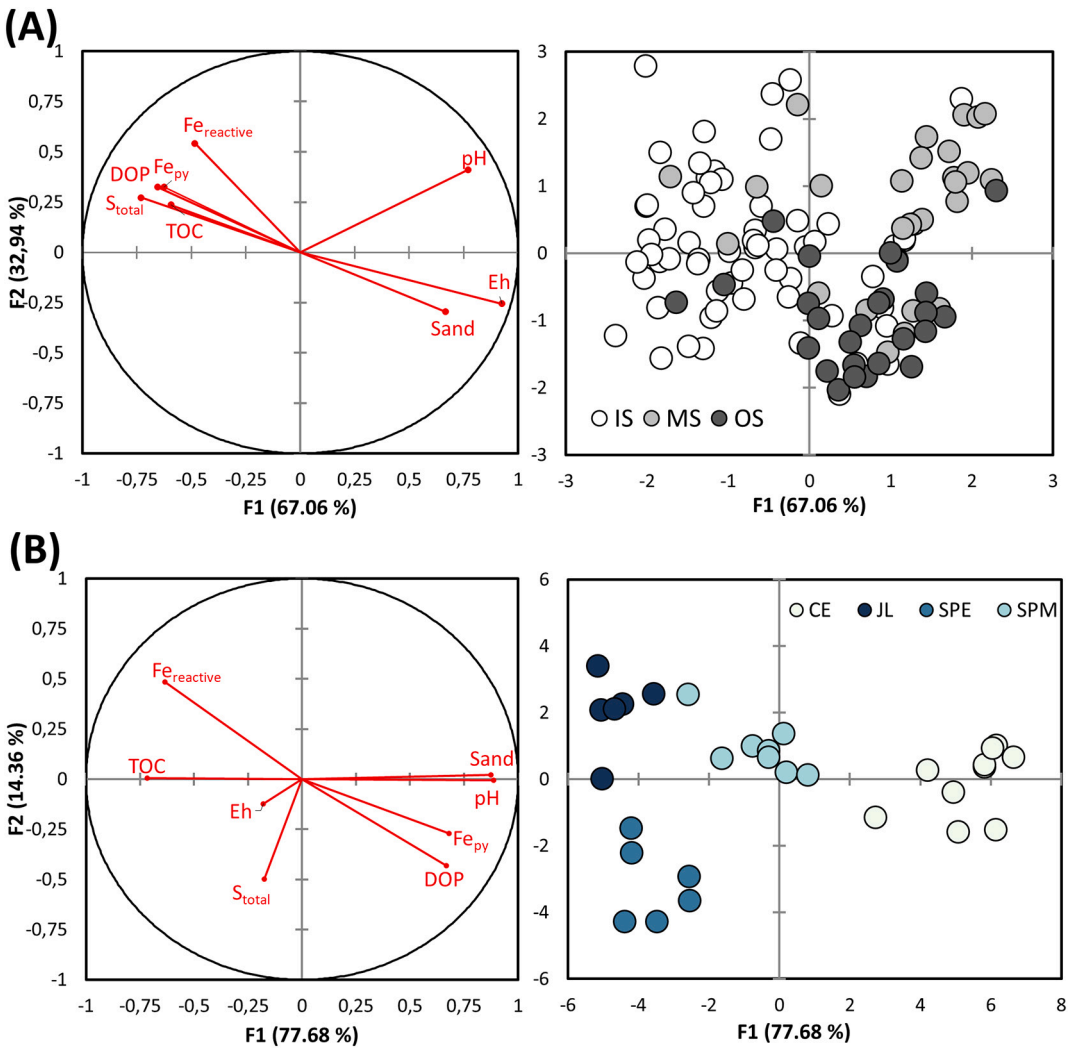

Fig. 3. A) Discriminant analysis for the sections of the Ria (IS – Inner section, MS – middle section, OS – outer section) and B) salt marsh soils with sediment and soil characteristics.

15–35 cm (Table 2). In salt marsh soils, DOP ranged from very low values in JL2 (0.6 ± 0.2%) to very high values in the lower salt marsh (SPE2 15–35 cm; 75.1 ± 11.2%) and soils of *Spartina*-dominated higher salt marsh (SPM2 15–45 cm, 83.4 ± 1.0%, Table 2). Deeper soil samples from SPM2 15–45 cm, SPE2 15–35 cm, and CE channel samples showed higher DOP levels (DOP >75%), compared with those found in SPM1 0–3 cm, SPE1 0–3 cm, and JL and JL2 (Table 2). The DA showed a clear differentiation between CE and the plant-covered sites (SPE, JL, and SPM), with higher pH, sand, $Fe_{py,}$ and DOP values. In contrast, plant-covered sites showed higher TOC, $Fe_{reactive}$, and S_{total} (Fig. 3B). Comparing plant-covered sites, SPM was associated with lower TOC and higher sand contents and pH, whereas JL was mostly associated with higher reactive Fe, and SPE was mostly associated with higher Eh and S_{total}.

3.4. Pyrite distribution and morphology

A total number of 1036 pyrites were observed by SEM in sediment and soil samples (Table 3). Individual framboidal pyrites (578 observations) and individual pyrite microcrystals (219 observations) were the dominant morphologies, followed by framboidal pyrites within organic structures (such as diatom frustules, 68 observations), whereas pyrites within plant tissues were less common (34 observations; Fig. 6, Table 3).

Bottom sediments showed notably lower pyrites (319 observations) than salt marsh soils (717 observations). In the bottom sediments, framboidal pyrites and individual microcrystals were the most commonly observed category (Fig. 4, Table 3). Moreover, their

Table 3
Pyrite morphologies in the studied environments of the Ria de Ortigueira.

Sample	Single crystals	Framboids	Clusters	Plant tissues	Diatom frustules
		Bottom sediments			
IS	0	112	0	9	0
MS	158	15	0	4	0
OS	21	0	0	0	0
		Low salt marsh soils			
SPE 0–3 cm	0	12	8	0	0
SPE 15–35 cm	0	65	117	11	0
		salt marsh channel			
CE	38	52	2	10	1
		High salt marsh soils			
SPM 0–3 cm	0	163	1	0	12
SPM2 15–45 cm	2	150	9	0	55
JL 0–3 cm	0	7	0	0	0
JL 15–35 cm	0	2	0	0	0
Total	219	578	137	34	68

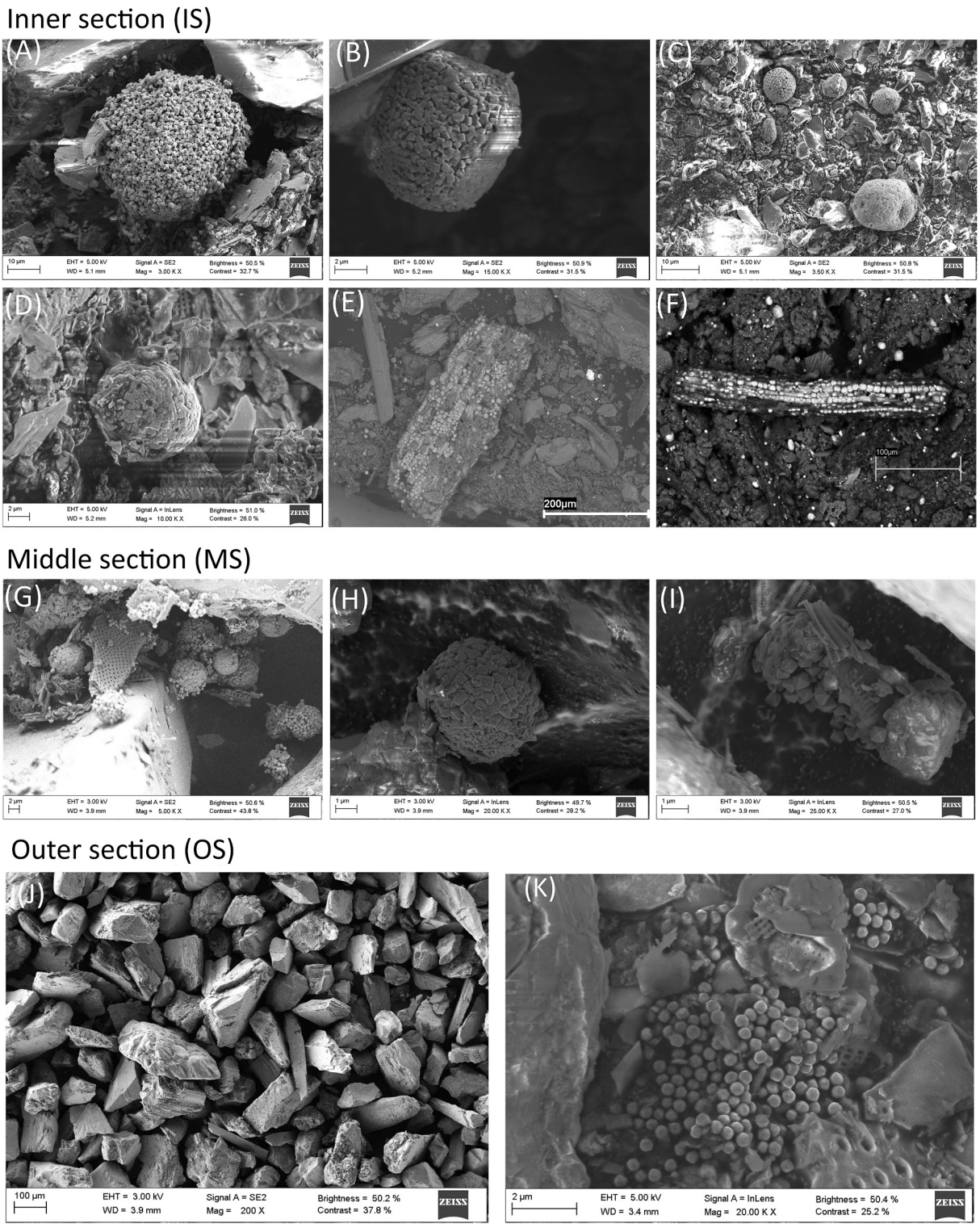

Fig. 4. Microphotographs of pyrites from the bottom sediments of the Ria de Ortigueira. Framboidal pyrites from the inner section (A-F). Pyrites filling plant tissues (E and F). Pyrites from the middle section (G-I) and from the outer section (J-K), where the dense fraction is formed mainly by siliciclastic sediments (J) and very low content of pyrites (K). Pyrites from the bottom sediments showing octahedral (A, I) and cubic (B) habits. However, unlike the pyrites observed in marsh soils (Fig. 6), pyrite framboids in the sediments of the Ria are formed by microcrystals with poorly defined facets, edges, and vertices and cavities indicating that the framboids have been under unstable conditions.

morphology showed poorly defined facets, edges, and vertices (Fig. 4). MS and OS showed poorly defined pyrite microcrystals with cubic, pyritohedral (dodecahedral), and octahedral habit (Fig. 4), whereas IS samples also showed framboidal pyrites incorporated into plant tissues (Fig. 4E and F: Table 2). Framboids were only observed in IS and MS, while at OS, a low number of isolated pyrite microcrystals were observed (21 observations, Fig. 4J and K).

A greater number of pyrites were counted in salt marsh soils, corresponding to 78% of the total number of observations, as well as a wider diversity of sizes and morphologies (Table 3; Fig. 5). For example,

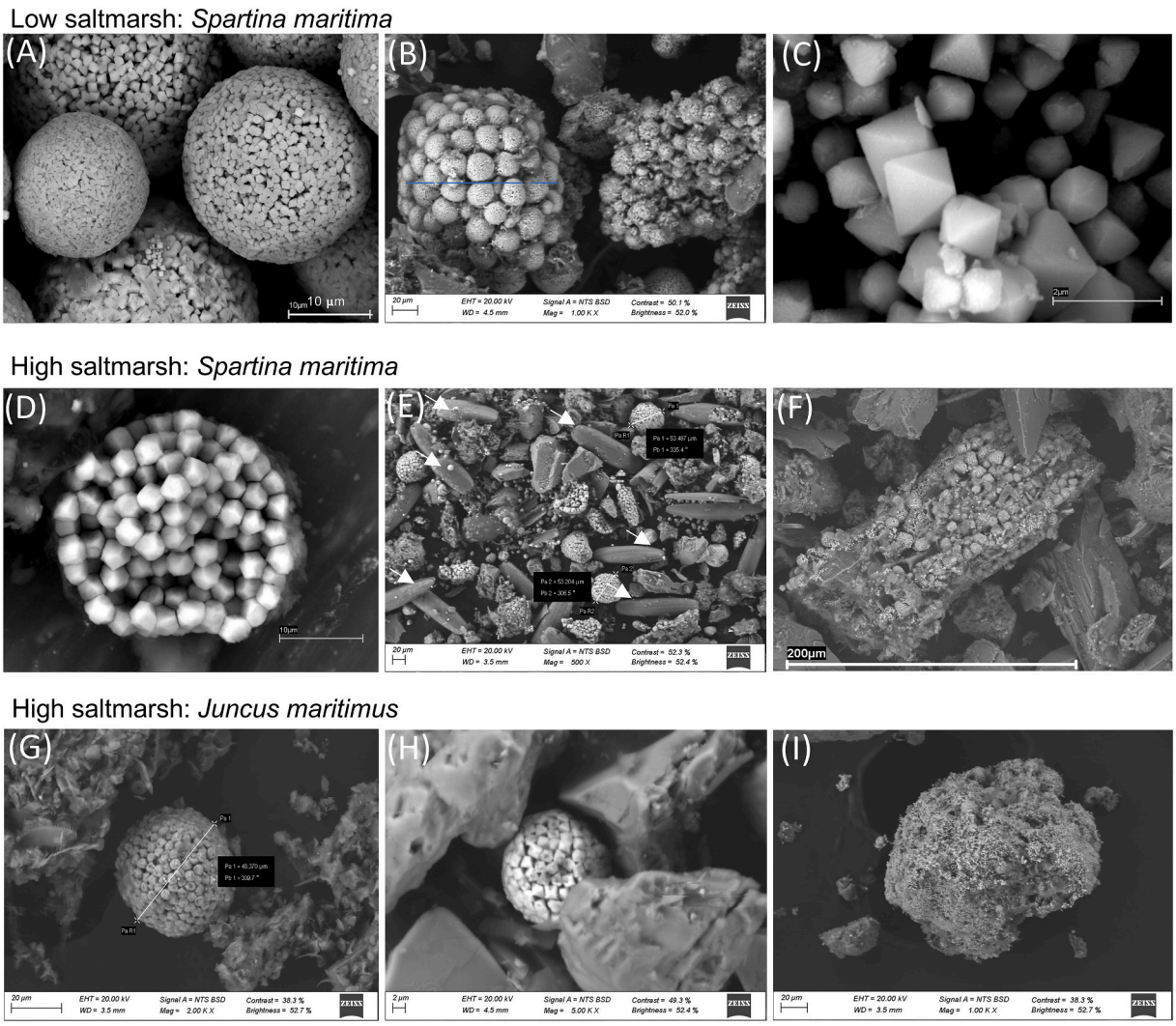

Fig. 5. Microphotographs of pyrites from salt marsh soils. Pyrites from lower salt marsh soils (SPE) covered by *Spartina maritima* (A-C). Framboids from SPE 0–3 cm formed by spherical framboids of variable sizes (A). Large pyrite polyframboids (>100 µm) from the upper portion of soil in SPE1 0–3 cm (B). Individual pyrites microcrystal with well-defined surfaces (C). Pyrites from higher salt marsh soils (SPM) colonized by *Spartina maritima (D—F)*. Framboid formed by pyrite microcrystals with a well-defined dodecahedral habit (D). High abundance of framboids and filled diatom frustules in SPM soil (E). Large framboid cluster within plant tissues in SPE2 15–35 cm soil (F). Pyrites from higher salt marsh soils colonized by *Juncus maritimus* (Sea rush, JL samples) (G-I). Individual framboidal pyrite from salt marsh soil JL1 0–3 cm (G). Framboidal (H) and polyframboidal (I) pyrites from the deep layer of JL2 (15-35 cm) with poorly defined crystals.

in addition to isolated framboids and crystals, polyframboids/clusters formed by the aggregation of several framboids were commonly found in salt marsh soils, as framboids formed in diatom frustules and plant tissues (Fig. 5). Additionally, larger framboids and microcrystals with well-defined facets and edges were observed in salt marshes, especially in the deeper soil layers colonized by *Spartina maritima* (both in the higher and lower salt marsh, i.e., SPE2 15–30 and SPM2 15–45 cm).

Most of the framboids observed in salt marsh soils were formed by tens to hundreds of pyrite microcrystals with well-defined habits (Fig. 5). However, in some cases, particularly in the upper layers of soils under *Spartina maritima* and *Juncus maritimus*, microcrystals showed clear signs of alteration, such as poorly defined edges and facets or clear evidence of dissolution or corrosion (Fig. 6).

3.5. Size distribution of framboidal pyrites

Individual framboid sizes ranged between 2 and 85 µm (Table 4). The highest geometric mean ($\bar{x}$*) corresponded to sample SPM2 15–35 cm ($\bar{x}$* = 54.8 µm), followed by samples from JL2 15–35 cm ($\bar{x}$* = 37.7 µm), SPE2 15–35 cm ($\bar{x}$* = 35.8 µm), and SPE1 0–3 cm ($\bar{x}$* = 21.9 µm). Sediments from the Ria and the salt marsh channel (CE) showed smaller framboids (< 10 µm).

Most framboids (44%) were medium-sized (3–30 µm) and mainly associated with organic structures, such as diatom frustules and plant tissues (Table 4; Fig. 7). Large framboids (i.e., those with diameters >30 µm; Rickard, 2019a, 2019b, Wilkin et al., 1996) accounted for 34% and were only found in salt marsh soils (Fig. 7).

4. Discussion

4.1. Size, morphology, and stability of framboids in salt marsh soils and sediments

Framboids are the main pyrite morphology in modern sedimentary environments, such as marine sediments and coastal marsh soils (Wilkin et al., 1996; Wilkin and Barnes, 1997). The size of framboidal pyrites observed in sediments from the Ria follows the range of pyrites observed in most marine sediments, i.e., from 5 to 10 µm (Wilkin et al., 1996; Roychoudhury et al., 2003; Rickard, 2012), whereas pyrites found in salt marsh soils were much larger (arithmetic mean values ranging from 10.2

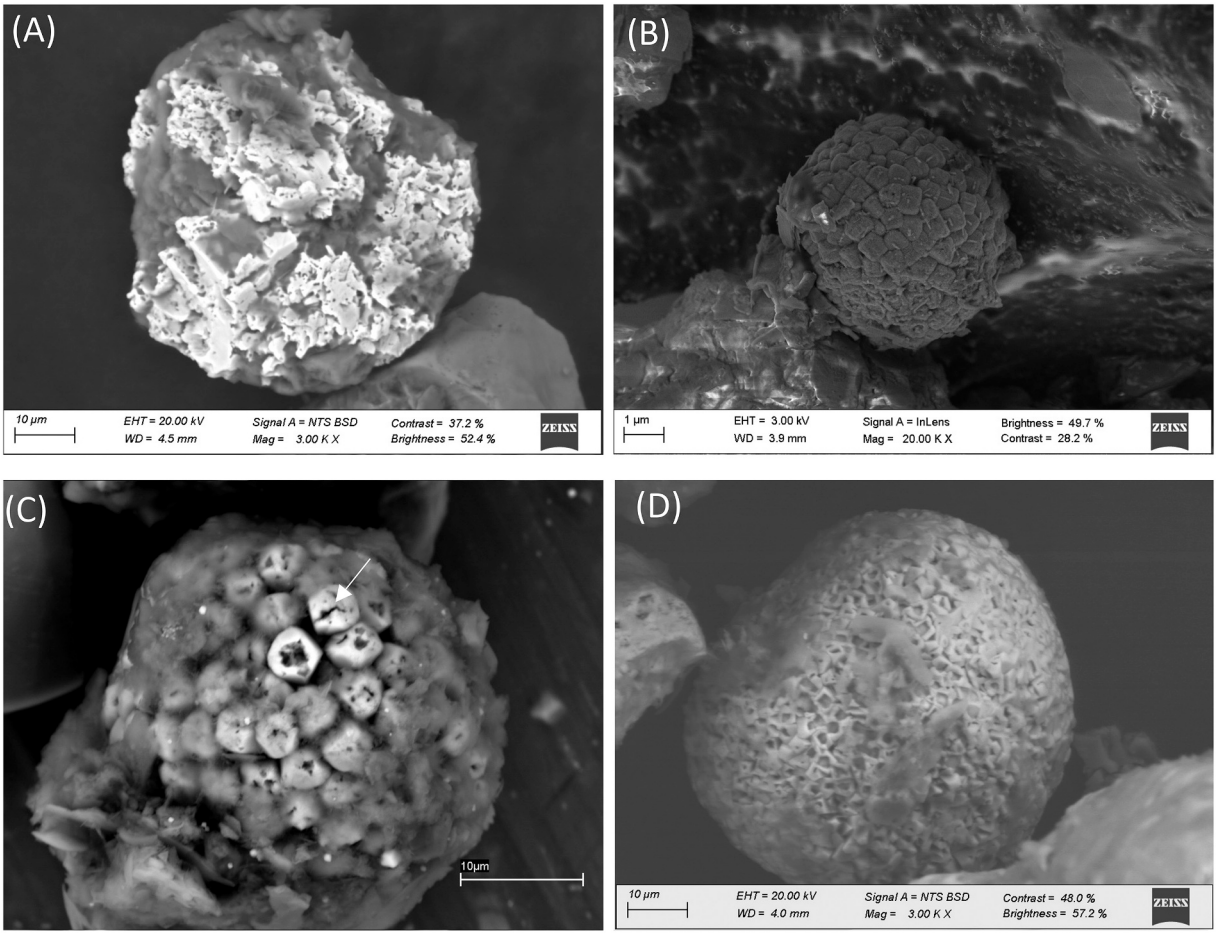

Fig. 6. Framboid with clear evidence of corrosion from JL 0–3 cm (A). Framboids from JL 15–35 cm showing poorly defined crystals (B). Altered framboids from the surface of lower salt marsh soil (SPE 0–3 cm) (C). Framboid with signs of pitting (D).

Table 4
Framboid diameters expressed as arithmetic and geometric statistical parameters.

Samples	n	$\bar{x}$	σ	$\bar{x}^*$	σ*	máx.**	min**
		µm					
Bottom sediments - Ría							
IS	112	10.7	6.5	9.1	1.8	29	3
MS	15	7.2	4.2	6.3	1.7	18	2
OS	n.o	n.o	n.o	n.o	n.o	n.o	n.o
Low salt marsh soils							
SPE 0–3 cm	12	25.7	15.7	21.9	1.8	71	7
SPE2 15–35 cm	65	37.4	11.2	35.8	1.3	61	21
Salt marsh channel							
CE	52	9.1	5.5	7.8	1.7	23	3
High salt marsh soils							
SPM 0–3 cm	163	10.2	2.9	9.8	1.3	17	6
SPM 15–45 cm	150	56.1	12.3	54.8	1.2	79	38
JL 0–3 cm	7	21.5	10.2	19.4	1.6	50	8
JL 15–35 cm	2	40.9	17.3	37.7	1.5	85	17

n: number of observations; n.o: not observed; $\bar{x}^*$: geometric mean; σ*: geometric standard deviation.

to 56.1 µm; Fig. 7). In addition, framboids in the deeper layers of salt marsh soils were significantly larger than those in the upper layers ($p = 0.038$, $U = 0.000$), showing a pattern of increasing pyrite size with depth (Figs. 7, 8).

These observations suggest that framboids may experience secondary growth upon burial, as observed in other salt marshes (e.g., Great salt marsh, USA) and marine sediments (e.g., continental slope in Peru), with a positive correlation between framboid diameter and depth and suggesting continuous growth (Wilkin et al., 1996; Wilkin and Barnes, 1997). Growth of pyrite microcrystals requires contact with a supersaturated solution containing reduced Fe and S forms (i.e., Fe^{2+}, HS^-, S^{2-}) (Wilkin et al., 1996; Kozina et al., 2018; Rickard, 2019b). Thus, salt marsh soils provide the required conditions for framboid growth due to the generally high rates of sulfate reduction, stimulated by labile organic matter input by plants (Howarth, 1979). Additionally, the frequent exposure of soils to the atmosphere and the oxidizing activity by plants may fuel pyritization (Luther et al., 1982) as dissolved hydrogen sulfide can be partially oxidized to polysulfides or other sulfur species, with intermediate oxidation states below the oxic-anoxic interface (see Wilkin et al., 1996).

Framboid growth time can range from 5 days for sizes of approximately ~5 µm to around 2.2 years for large framboids with diameters of ~80 µm (Rickard, 2019a). Other authors have proposed that complete framboid formation requires approximately five years (Wilkin et al., 1996; Schieber and Schimmelmann, 2007). Considering a sedimentation rate of 1 cm $year^{-1}$ in the study site (Lorenzo et al., 2007), the largest framboids observed in the lower salt marsh soil could have reached their size in the upper 5–10 cm, compared with the soil surface (i.e., 0–3 cm) from higher salt marshes (Table 4). These surface layers constitute the most geochemically active layers in terms of biological activity, density of live roots, burrows, and sulfate-reducing activity (Otero and Macías, 2002; Bahr et al., 2005). These conditions are typical of lower salt marsh soils, as well as of higher salt marsh soils dominated by *Spartina maritima*, where higher Fe pyritization (DOP: 30–80%; Table 2) than in other salt marsh areas (e.g., tidal flats) has been reported (for further

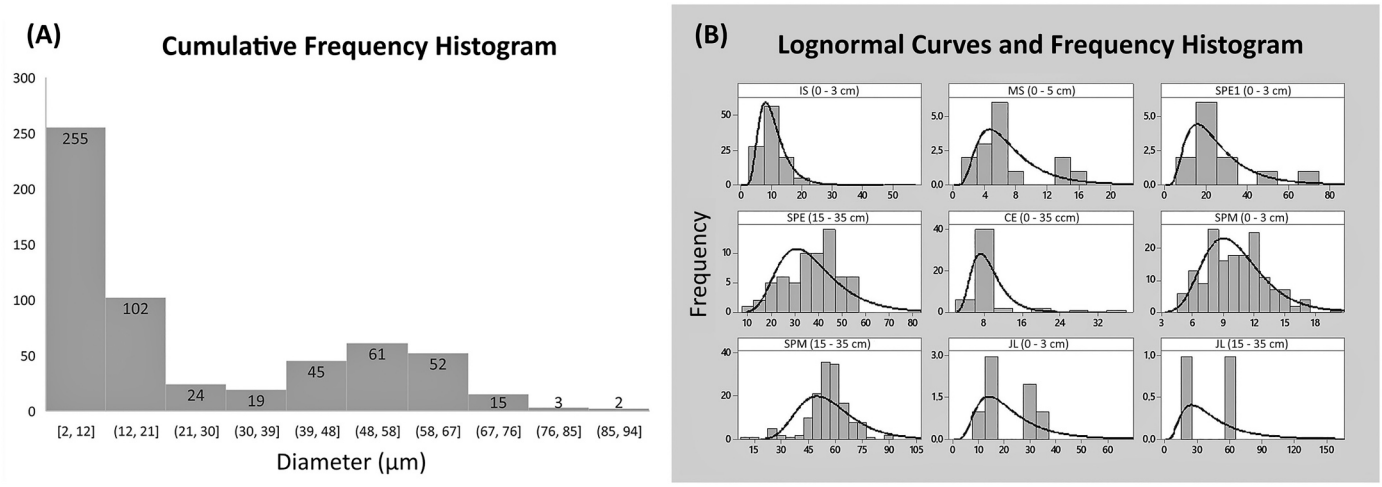

Fig. 7. Size distribution histograms for framboids in the salt marsh-*ria* system. A) Individual sample histograms. B) Size distribution histogram for framboidal pyrites (except for OS due to lack of specimens).

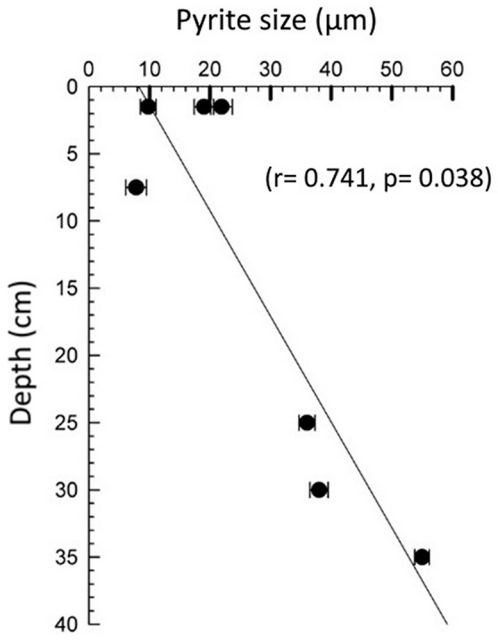

Fig. 8. Correlation between framboidal pyrite size and depth in salt marsh soils.

details, see Otero and Macías, 2003).

Framboidal pyrites are composed of 10^2–10^7 microcrystals, usually around 10^4, with sizes ranging from 0.1 to 2 µm and with variable morphologies (cubic, octahedral, or dodecahedral; Rickard, 2012). Microcrystal morphology and size are related to the conditions in which pyrites are formed. Thus, framboids composed of small microcrystals (~0.1 µm) and poorly defined habits indicate a rapid formation, usually under euxinic water columns, such as those of the Dead Sea (Wilkin et al., 1996). On the other hand, the formation of framboids composed of cubic and pyritohedral (dodecahedral) euhedral crystals with well-defined facets and vertices require more extended periods and super-saturated interstitial waters as in anoxic sediments below oxic waters (Raiswell and Berner, 1985; Wang et al., 2013). Well-defined octahedral morphologies were mainly observed in deeper soil samples from areas with *Spartina* (SPM, SPE; Fig. 5), with most of the framboids observed in surface layers (SPE1 0–3 cm) of small-sized microcrystals (Fig. 5A). These observations are indicative of the rapid formation of small-sized pyrite microcrystals in the SPE1 0–3 cm, consistently with the biogeochemical conditions of the surface layers of lower salt marsh soils, i.e., high Eh values (Table 1) and low sulfate reduction rates, as indicated by DOP (Table 2; see Canfield et al., 1992).

A significant number of framboidal pyrites were found clustered into polyframboids or within biological structures (Table 3). However, the origin of polyframboids remains poorly studied, and their presence is uncommon in ancient and modern sedimentary environments (Lin et al., 2016). Nevertheless, clusters were present in most salt marsh samples (JL, SPE, and SPM; Table 3). The observed polyframboids were composed of 13–85 framboids, sometimes of similar sizes (~15 µm; Table 4) and sometimes of heterogeneous sizes (Fig. 5B). On the other hand, pyrites within biological structures such as plant remains or diatom frustules are frequently observed in marine sediments (Otero et al., 2013; Otero et al., 2014; Kozina et al., 2018). In the Ria de Ortigueira, these observations were widespread in the studied salt marsh soils (Fig. 5C).

Many studies on intertidal soils or coastal sediments usually consider the >63 µm fraction, i.e. the sand size fraction, as poorly reactive (Krumgalz et al., 1992; Carral et al., 1995; Stone and Droppo, 1996). However, previous studies have evidenced that the coarse sand fraction (>100 µm) may represent a fairly reactive fraction with 10–45% of the total Fe and trace metal contents, since it may contain pyrites (Otero et al., 2013). In sulfidic sediments, most of the Fe and potentially toxic elements (e.g., Cd, Hg, Pb) are found associated with the pyritic fraction (Huerta-Díaz and Morse, 1992), which is highly reactive (concerning both formation and degradation) within short periods (i.e., days; Morse and Mackenzie, 1990; Otero and Macías, 2002; Otero et al., 2006). Pyrite oxidation in intertidal substrates involves acidification and release of the associated potentially toxic elements into interstitial waters (for further details, see Otero, 2000; Otero and Macías, 2003; Otero et al., 2006).

Alteration of pyrite microcrystals occurs either by dissolution, when pyrite is found under unsaturated solution, or by oxidation (Rickard, 1970; Schallreuter, 1984; Rickard, 2012). Both processes seem to occur in the study area, especially in the deeper layers in JL2 15–30 cm (Fig. 6), under suboxic redox conditions (mean Eh ~150 mV; see also Otero and Macías, 2003). In fact, sulfate reduction was negligible, as evidenced by the low concentrations of pyritic Fe (Table 2). Likewise, under alternating redox conditions (i.e., seasonal changes, soils/sediments surface layers), pyrite may be destroyed by oxidation (Ding et al., 2014). The hydroperiod that promotes tidal flooding in salt marsh soils is subjected to temporal variations in tide regimes and seasonal cycles. Previous studies have shown significant decreases of Fe-pyrite in salt

marsh soils during the summer, when rainfall substantially decreases (Kostka and Luther, 1995; Otero and Macías, 2002). The pyrite corrosion observed by SEM images (Fig. 8) corroborates the oscillating redox conditions in salt marsh environments.

4.2. Distribution of framboidal pyrites in the salt marsh-ria system

The available information on the number and size of framboidal pyrites in salt marsh soils and sediments is scarce, and no information for the Galician rias is available (Morse and Mackenzie, 1990; Huerta-Díaz and Morse, 1992). Rickard (2015, 2019b) highlighted the global importance of pyrite framboids as one of the most abundant minerals on Earth, with up to $\sim 10^{30}$ framboids, or about 10^9 times the number of sand grains, at a forming rate of around 10^{14} per second. Vallentyne (1963), studying lake sediments in the US, isolated 10^5 framboids per gram of dry sediment, corresponding to a pyrite concentration of 0.2%. More recently, Wilkin et al. (1996) performed a more detailed study of framboid sizes and abundance in sediments from different marine environments (i.e., euxinic and oxic/dysoxic environments, ancient sediments, and salt marsh soils) and registered mean quantities of $10^{7.7\pm0.5}$ framboids ($\sim$ 42–452 μmol g^{-1} of pyrite).

Our study showed values ranging between 3×10^2 pyrites in soils with oxic/suboxic conditions (e.g., higher salt marsh dominated by *Juncus maritimus)* to 7×10^6 framboids in the ria sediments, salt marsh channels, and higher marsh soils occupied by *Spartina maritima*. These results show that intensely pyritized environments with high pyrite contents, such as SPM2 (3.81% pyrite) and SPE2 (2.76% pyrite), did not show the highest framboid numbers (Table 5). The reason for this lies in the framboid sizes within each site. Therefore, our calculations were made considering the mean framboid size at each site (Table 5) instead of a single mean value. In samples SPM2 15–45 cm and SPE2 15–35 cm, the mean diameter was 4 to 5 times higher than the largest size in other areas (Table 4). Therefore, the number of framboids does not seem suitable for correlating with redox conditions or pyritization intensity in coastal environments.

4.3. Salt marsh systems as a pyrite-rich system

Pyritic Fe concentrations and DOP values varied widely in salt marsh soils in the Ria de Ortigueira (Fe_{py}: 1.3 ± 0.2 to 320 ± 40.3 μmol g^{-1}; DOP: 0.5 ± 0.2 to 83.4 ± 1.0%; Table 6), which follow the variability in redox conditions (Table 1). The lower salt marsh showed significantly higher Fe_{py} values than those previously registered for anoxic or euxinic marine environments (Table 6) and higher than those found in the bottom sediments of the Ria ($p < 0.005$; U = 44.00; Table 5).

These results support the hypothesis that coastal salt marshes may act as a biogeochemical reactor (Anschutz et al., 2009; Palomo et al., 2013), where pyrite content in soils and degrees of Fe pyritization are among the highest in marine environments (Table 6). Moreover, our data evidence that intertidal environments, e.g., lower salt marsh soils, show geochemical conditions that promote rapid pyritization; therefore, pyrite may be considered one of the most abundant authigenic mineral in these ecosystems (Howarth and Teal, 1979; Howarth, 1984; Otero et al., 2009a, 2009b; Rickard, 2019a; see reactions 2–5). Indeed, previous studies have demonstrated high pyrite contents in salt marsh soils, particularly in areas covered by *Spartina* (Howarth and Teal, 1979; Kostka and Luther III, 1994; Otero and Macías, 2002). In the present study, pyrite contents were especially high in soils under *Spartina maritima* (Table 6). *Spartina maritima* is a pioneer species capable of colonizing lower salt marsh soils, characterized by high H_2S concentration, which is toxic for most plant species (Sánchez et al., 1997; Otero, 2000). In higher salt marshes, *Spartina maritima* is found in microdepressions that remain permanently flooded and where geochemical conditions are similar to those of lower salt marshes (Sánchez et al., 1998; Otero and Macías, 2003).

Additionally, *Spartina maritima* can enhance O_2 diffusion into the soil through their root systems, thus generating oxic microenvironments where poorly crystalline Fe oxyhydroxides (e.g., lepidocrocite) precipitate. Contrastingly, their roots secrete labile organic compounds, such as low-molecular-weight organic acids and carbohydrates, fuelling sulfate-reduction (Mendelssohn and Kuhn, 2003; Hines, 1991). This capacity to produce alternating redox conditions promotes the oxidation of dissolved H_2S to zero-valent sulfur species (S^0) and the formation of polysulfides, leading to direct pyrite precipitation (see eq. 5; Rickard, 1975; Howarth and Teal, 1979).

Higher salt marsh soils colonized by *Juncus maritimus,* although marked by high contents of organic C (as high as 9.73%) and $Fe_{reactive}$ (291.8 ± 67.9 μmol $g^{-1;}$ Table 2), showed lower concentrations of Fe_{py} (1.3 ± 0.2 μmol g^{-1}; Table 2). Considering that *Juncus* occupies most of the higher salt marsh (Sánchez, 1995), our results suggest that the progressive terrestrification of salt marsh environments may lead to lower pyritization, with the consequent mobilization of metals associated with the pyritic fraction.

Table 6
Reactive and pyrite-Fe contents (%; mean ± SD; median is indicated within parentheses) in soil and sediments from Ria de Ortigueira compared with other marine environments.

Site	$Fe_{reactive}$	Fe_{py}	Reference
Low salt marsh soils- ría de Ortigueira (n = 6)	0.69 ± 0.89 (0.50)	1.04 ± 1.34 (0.52)	*This study*
High salt marsh soils ría de Ortigueira (n = 6)	1.06 ± 0.65 (1.12)	0.67 ± 0.83 (0.42)	*This study*
Sediments-ría de Ortigueira (*n* = 19)	0.77 ± 0.42 (0.60)	0.17 ± 0.25 (0.21)	*This study*
Surface sediments-*Ría de Vigo* (Galicia-NW Spain) (*n* = 24)	1.10 ± 0.40	0.61 ± 0.1	Otero et al., 2009; Ramírez-Pérez et al., 2020
Continental margin (*n* = 46)	0.73 ± 0.34	0.09 ± 0.40	Raiswell and Canfield, 1998
Deep sea (*n* = 56)	0.66 ± 0.32	0.06 ± 0.10	Raiswell and Canfield, 1998
Dysoxic sediments (*n* = 26)	0.36 ± 0.34	0.57 ± 0.32	Raiswell and Canfield, 1998
Euxinic sediments. Black sea (*n* = 45)	0.16 ± 0.11	1.15 ± 0.39	Anderson and Raiswell, 2004

Table 5
Concentration of pyritic Fe (Fe_{py}), framboid size, and number of framboids in the studied salt marsh-*ria* system.

	Bottom Sediments-Ría			Salt marsh soils						
	IS	MS	OS	SPE 0–3 cm	SPE 15–35 cm	CE	SPM 0–3 cm	SPM2 15–45 cm	JL 0–3 cm	JL 15–35 cm
Fe-py (μ mol g^{-1})	71.9	11.3	2.4	21.1	231	263	81	320	2.10	1.30
% pyrite	0.81	0.13	0.03	0.25	2.76	3.16	0.97	3.81	0.03	0.02
$\bar{x}^*$ (μm)	9.1	6.3	n.d.	21.9	35.8	7.8	9.8	54.8	19.4	37.7
m_p (g)	2.00E-09	7.00E-10	n.d.	3.00E-08	1.00E-07	1.00E-09	3.00E-09	4.00E-07	2.00E-08	1.00E-07
framboides g^{-1}	4.00E+06	2.00E+06	n.d.	5.00E+04	4.00E+05	7.00E+06	7.00E+06	8.00E+04	2.00E+04	3.00E+02

N: number of observations; n.o: not observed; $\bar{x}^*$: geometric mean; σ*: geometric standard deviation.

4.4. Pyrite transport in the salt marsh-ria system

Pyrite contents in the bottom sediments of the Ria (Fe_{py}: 0.16 ± 0.26%; ~30 μmol g^{-1}; Table 2) were around 6-fold lower than those observed in the lower salt marsh soils. These contents were also substantially lower than those reported for other coastal sediments worldwide (Table 6; see Raiswell and Canfield, 1998; Rickard, 2012). The low pyrite contents in MS and OS were similar to those observed in sediments from the continental margin and deep ocean (0.09 ± 0.40% and 0.06 ± 0.10%, respectively; Table 6). These are generally poor in organic matter and have a low degree of pyritization (Berner, 1970). However, IS showed substantially higher pyrite contents (0.40 ± 0.28%; 71.9 ± 50 μmol g^{-1}; Table 2). Moreover, the physicochemical conditions and residual velocities favored the higher pyrite contents in IS. The residual velocities in IS were weak throughout the water column (around 0.01 ms^{-1}; Fig. 2 A,B), one order of magnitude lower than in MS. This fact could be partly due to the low capacity of the tide to generate residual currents given the specific geometrical configuration of this area, which is wider than MS and shows large intertidal areas. Thus, the reduced river discharges generate a weak downstream flow restricted to its central channel, favoring a higher pyrite content (Table 2). Additionally, IS's suboxic/anoxic conditions also favored pyrite framboid formation as observed by SEM (Fig. 4). However, the frequent signs of alteration (i.e., poorly defined facets, edges, and vertices, presence of cavities, signs of dissolution and corrosion; Fig. 4) seem to suggest that pyrites are under unstable conditions. These signs of alteration could result from bioturbation (Ferreira et al., 2007), but could also be due to alterations occurred during transport of pyrites from marsh soils to the sediments of the Ria, leading to the hypothesis that part of the pyrites present in the sediments of the Ria have an allochthonous origin.

Otero et al. (2014) found abnormally high pyrite contents in sandy sediments in a mangrove channel in Cardoso Island, SE Brazil. The authors concluded that pyrites formed in the adjacent mangrove soils were transported to the channel by tidal action during ebb tides, leading to overpyritization of the sandy sediments. Our results seem to suggest a similar situation between the salt marsh and sediments in sections IS and MS, where some pyrites seemed to have come from the progressive collapse of salt marsh channels rather than having been formed in situ. As shown in Fig. 4, sediments showed framboidal pyrites within plant tissues, which could corroborate their origin in the adjacent salt marshes, as was observed in studies carried out on soils of the same salt marsh (Otero, 2000), although they could also be pyrite-free plant debris that had been transported to the sediments of the Ria and undergone post-depositional pyritization. However, the regression line for total organic Carbon (TOC) vs Total for sectors IS and MS intercepted the y axis at 0.10% (Total S = 0.10 + 0.22 TOC, $r^2 = 0.557$, $n = 91$), which suggests that the sediments of the Ria de Ortigueira show overpyritization (Raiswell and Berner, 1985), thus supporting the initial hypothesis that part of the pyrites present in sediments may come from salt marsh soils (Otero et al., 2014).

Lower salt marsh soils are subjected to intense tidal influence and showed a high degree of pyritization (Table 2). Moreover, the lower parts of the channels in the higher salt marsh can also show high degrees of pyritization (Lambais et al., 2008). Both sites (channels and lower salt marsh) showed clear signs of erosion in the study area due to sea-level rise (2–3 mm y^{-} for the Atlantic coast; Climate Change Post, 2020). The collapse of channel banks associated with tidal movements leads to the transport of eroded soil and sediments material from salt marshes towards the Ria through the dense drainage network within the salt marsh (see also Valiela, 2015; Valiela et al., 2018). The importance of this process is particularly relevant in IS and MS, as these sections are in close contact with adjacent salt marshes (e.g., salt marshes of Mera and Esteiro; Fig. 1).

In addition to these general patterns, other complex processes should also be analyzed to describe pyrite transport in this Ria. In particular, it is important to note the presence of a counterclockwise eddy in the area with the strongest residual circulation in the outer portion of MS. This combination with the previously described general pattern could significantly affect pyrite distribution. The greater amounts of pyrite present in IS are subject to low residual downstream velocities (Fig. 2) that hinder its transport to MS. In addition, although MS shows a greater residual circulation (Fig. 2), the transport of pyrite framboids is limited by the existence of a residual eddy, which may preclude to some extent their flow through the narrow section separating MS from OS, therefore preventing their presence in OS.

In this sense, a different situation was observed in OS, where the low pyritization degrees were consistent with the oxic conditions (Eh = 311 ± 134 mV; Table 1) and the low TOC contents (0.57 ± 0.5%; Table 1). Under such conditions, sulfate reduction is low and associated with microsites enriched in labile organic matter. Therefore, the level of supersaturation necessary for pyrite precipitation should be low, allowing for the formation of only isolated pyrite microcrystals. The formation of framboidal pyrites, on the other hand, requires supersaturation values around 11 orders of magnitude higher than the equilibrium values (Rickard, 2012).

Additionally, the hydrological study showed that IS acts as a sink for pyrites. Except for the inner section, most sections of OS showed weaker velocities (around 0.1 m s^{-1}) throughout its central channel in the surface layer, decreasing to 0.02 m s^{-1} in the bottom layers (Fig. 2B). In addition, the overall pattern of a positive estuarine circulation led to the greater importance of river discharge over the tide for generating net circulation in the IS. Thus, the higher amounts of pyrite in IS compared with the remaining sections are related to the slow current velocities (Fig. 2C), which would limit the transport towards MS, particularly of larger framboids. Moreover, the bottleneck formed by the Ria between MS and OS (Fig. 2) promotes the formation of an eddy, which could act as a plug that reduces sediment output from MS towards OS.

5. Conclusions

The pyritization of bottom sediments at the Ria de Ortigueira was significantly lower than inadjacent lower salt marsh soils. Conversely, the number of framboidal pyrites per gram of sediment was higher in sediments from the Ria than in salt marsh soils, ranging from 2×10^6 to 4×10^6 in sediments and from 3×10^2 to 7×10^6 in salt marsh soils, although their sizes were significantly smaller. These data evidence that the number of pyrite framboids is not a good indicator of the degree of Fe pyritization in salt marsh sediments and soils.

The results show that soils from lower marshes colonized by *Spartina maritima* (i.e. labile organic matter, bioturbation, high sulfate reduction activity, partial oxidation of H_2S) constitute one of the geochemical environments where Fe pyritization occurs at a higher intensity compared with other marine environments. The intense Fe pyritization observed in the lower marsh mainly produces framboidal pyrites and large polyframboids, whose size increases with depth. The highly significant correlation observed between pyrite size and depth suggests that framboids experience secondary growth upon burial.

On the other hand, the visible signs observed in framboids from sediments at the bottom of the Ria de Ortigueira, together with the observation of pyrite-filled plant debris in sediments of the Ria and with the intersection of the regression line for the TOC vs Total S relation with the Y axis, seem to suggest that these are exported from salt marsh soils towards the nearby seabed, where geochemical conditions promote their progressive dissolution. This process is expected to increase with time due to rising sea water levels, which promote the erosion of salt marsh soils (particularly in lower marshes). The massive output of pyrites towards coastal areas and their subsequent oxidization is a process that could affect the geochemical cycle of Fe and of other pyrite-associated metals (e.g. Cu, Pb, Zn, Hg, As, Co, etc).

In the case of the Ria de Ortigueira, the contrasting currents within the salt marsh-Ria system determine preferential sites to act as sinks for

pyrites in areas where this mineral is not formed but inherited from the surrounding eroded salt marshes. Furthermore, the weak residual currents in the inner section of the Ria, together with the presence of an eddy in the transition from the middle to the outer section, turn the inner section of the Ria de Ortigueira into a pyrite sink, preventing framboidal pyrites from being exported towards outer sections of the Ria.

Data availability statement

The data with which this article has been prepared are part of the doctoral thesis of Paulina Guevara (Space-temporal variability of the concentration of trace metals in soils and sediments in the Ria de Ortigueira in relation to the sources and residual dynamics of marine currents) and they can be accessed in the MINERVA repository of the University of Santiago de Compostela (https://minerva.usc.es/xmlui/?locale-attribute=gl).The data can also be available from the author (Xose L Otero: xl.otero@usc.es).

Declaration of Competing Interest

The authors declare the following financial interests/personal relationships which may be considered as potential competing interests:

Xose Luis Otero reports financial support was provided by Government of Galicia Department of Culture Education and Universities. Paulina Guevara reports financial support was provided by Universidad de Las Fuerzas Armadas de Ecuador. Rodrigo Carballo reports financial support was provided by Government of Galicia Department of Culture Education and Universities. Paulina Guevara reports was provided by Senescyt.

Acknowledgements

The authors are grateful to María José Santiso for her assistance with laboratory work. This work was funded by the Xunta de Galicia (Consellería de Educación, Universidade e Formación Profesional Axudas á consolidación e estruturación de unidades de investigación competitivas do SUG del Plan Galego IDT, Ambiosol Group ref. 2018-PG036). Paulina Guevara was in receipt of a predoctoral fellowship from the Senescyt and Universidad de las Fuerzas Armadas Program. The authors also would like to thank two anonymous reviewers for their valuable suggestions.

References

Aller, R., 1980. Diagenetic Processes near the Sediment-Water Interface of Long Island Sound. II. Fe and Mn. Adv. Geophys. 22, 351–415. https://doi.org/10.1016/S0065-2687(08)60068-0.

Anderson, T., Raiswell, R., 2004. Sources and mechanisms for the enrichment of highly reactive iron in euxinic Black Sea sediments. Am. J. Sci. 304 (3), 203–233.

Anschutz, P., Smith, T.M.A., Deborde, J., Bujan, S., Poirier, D., Lecroart, P., 2009. Tidal sands as biogeochemical reactors Estuarine, Costal and Shelf. Science 84, 84–90.

Bahr, M., Crump, B., Klepac-Ceraj, V., Teske, A., Sogin, M.L., Hobbie, J.E., 2005. Molecular characterization of sulfate-reducing bacteria in a New England salt marsh. Enviroment Microbiol 7 (8), 1175–1185. https://doi.org/10.1111/j.1462-2920.2005.00796.x.

Berner, R., 1967. Thermodynamic stability of sedimentary iron sulfides. Amer. J. Sci. 265 (265), 773–785. https://doi.org/10.2475/ajs.265.9.773.

Berner, R., 1970. Sedimentary pyrite formation. Am. J. Sci. 268 https://doi.org/10.2475/ajs.268.1.1, 261,1–23.

Bertness, M., Jeffere, R., Moller, L., 2005. Salt marsh erosion and restoration in south esth England. Journal of Aplied Ecology 844–851. https://doi.org/10.1111/j.1365-2664.2005.01080.x.

Cambardella, C.A., Gajda, A.M., Doran, J.W., Wienhold, B.J., Kettler, T.A., 2001. Estimation of Particulate and Total Organic Matter by Weight Loss-on-Ignition. In: Lal, R., Kimble, J.M., Follett, R.F., Stewart, B.A. (Eds.), Assessment Methods for Soil Carbon. Lewis Publishers, Boca Raton, FL, USA, pp. 349–359.

Canfield, D., Rainswell, R., Bottrell, S., 1992. The reactivity of sedimentary iron minerals toward sufide. Am. J. Sci. 292, 659–683. https://doi.org/10.2475/ajs.292.9.659.

Carral, E., Puente, X., Villares, R., Caballeira, A., 1995. Background heavy metals leveles in estuarine sediments and organisms in Galicia (NW Spain) as determined by modal analysis. Sci. Total Environ. 172 (2–3), 175–188. https://doi.org/10.1016/0048-9697(95)04788-3.

Climate Change Post, 2020. Sea Level Rise in Spain. Retrieved on 2020 from. https://www.climatechangepost.com/spain/coastal-floods/.

Ding, H., Yao, S., Chen, J., 2014. Authigenic pyrite formation and re-oxidation as an indicator of an unsteady-state redox sedimentary environment: evidence from the intertidal mangrove sediments of Hainan Island, China. Cont. Shelf Res. 78, 85–99. https://doi.org/10.1016/j.csr.2014.02.011.

Ferreira, T.O., Otero, X.L., Vidal-Torrado, P., Macías, M., 2007. Effects of bioturbation by root and crab activity on iron and sulfur biogeochemistry in mangrove substrate. Geoderma 142, 36e46.

Filgueiras, A., Prego, R., 2007. Biogeochemical Fluxes of Iron from rainwater, rivers and sewage to a Galician Ria (NW Iberian Peninsula). Natural versus anthropogenic contributions. Biogeochemistry 86, 319–329. https://doi.org/10.1007/s10533-007-9163-6.

Gee, G.W., Bauder, J.W., 1986. Particle-size Analysis. In: Methods Soil Anal., SSSA Book Series 383–411. https://doi.org/10.2136/sssabookser5.1.2ed.c15.

Giblin, A.E., Howarth, R.W., 1984. Porewater evidence for a dynamic sedimentary iron cycle in salt marshes. Limmol. Oceanogr. 29 (1), 47–66. https://doi.org/10.4319/lo.1984.29.1.0047.

Guevara, P., Perez-Alberti, A., Carballo, R., Sánchez, R., López, I., Otero, X.L., 2021. Impact of serpentinized peridotite mine waste on the composition and quality of sediments in the Ria de Ortigueira (Galicia, NW Spain). Mar. Pollut. Bull. 163, 111963. https://doi.org/10.1016/j.marpolbul.2020.111963.

Hines, M., 1991. The role of certain infauna and vascular plants in the mediation of redox reactions in marine sediments. Dev. Geochem. 6, 275–286. https://doi.org/10.1016/b978-444-88900-3.50031-x.

Howarth, R., 1984. The ecological significance of sulfur in the energy dynamics of salt marsh and coastal marine sediments. Biogeochemistry 1, 5–27.

Howarth, R., Teal, J., 1979. Sulfate reduction in a New England salt marsh. Limnol. Oceanogr. 24 (6), 999–1013. https://doi.org/10.4319/lo.1979.24.6.0999.

Howarth, R.W., 1979. Pyrite: its rapid formation in a salt marsh and its importance in ecosystem metabolism. Science 203 (4375), 49–51. https://doi.org/10.1126/science.203.4375.49.

Huerta-Díaz, M., Morse, J., 1992. Piritization of trace metals in anoxic marine sediments. Geochim. Cosmochim. Acta 56, 2681–2702. https://doi.org/10.1016/0016-7037(92)90353-K.

Kirwan, M.L., Mudd, S.M., 2012. Response of salt-marsh carbon accumulation to climate change. Nature 489, 550–553. https://doi.org/10.1038/nature11440.

Kostka, J., Luther, G., 1995. Seasonal cycling of Fe in saltmarsh sediments. Biogeochemistry 29, 159–181. https://doi.org/10.1007/BF00000230.

Kostka, J., Luther III, G., 1994. Partitioning and speciation of solid phase iron in salt marsh sediments. Geochimica et Cosmochimica 58 (7), 1701–1710. https://doi.org/10.1016/0016-7037(94)90531-2.

Kozina, N., Reykhard, L., Dara, O., Gordeev, V., 2018. Framboidal pyrite formation in the bottom sediments of the South Caspian Basin under conditions of hydrogen sulfide contamination. Russian Journal of Earth Sciences 18 (ES6003), 1–10. https://doi.org/10.2205/2018ES000639.

Krumgalz, B., Fainshtein, G., Cohen, A., 1992. Grain size effect on anthropogenic trace metal and organic matter distribution in marine sediments. Sci. Total Environ. 116 (1–2), 15–30. https://doi.org/10.1016/0048-9697(92)90362-V.

Lambais, M., Otero, X.L., Cury, J., 2008. Bacterial communities and biogeochemical transformations of iron and sulfur in a high saltmarsh soil profile. Soil Biol. Biochem. 40 (11), 2854–2864. https://doi.org/10.1016/j.soilbio.2008.08.014.

Lan, Y., Butler, E.C., 2014. Monitoring the transformation of mackinawite to greigite and pyrite on polymer supports. Appl. Geochem. 50, 1–6. https://doi.org/10.1016/j.apgeochem.2014.07.020.

Limpert, E., Stahe, W.A., 2011. Problems with using the Normal distribution – and Ways to Improve Quality and Efficiency of Data Analysis. PLoS One 6. https://doi.org/10.1371/journal.pone.0021403.

Lin, Q., Wang, J., Algeo, T., Sun, F., Lin, R., 2016. Enhanced framboidal pyrite formation related to anaerobic oxidation of methane in the sulfate-methane transition zone of the northern South China Sea. Mar. Geol. 379, 100–108. https://doi.org/10.1016/j.margeo.2016.05.016.

Lorenzo, F., Alonso, A., Pellicer, M.J., Pagés, J.L., Pérez-Arlucea, M., 2007. Historical analysis of heavy metal pollution in three estuaries on the North coast of Galicia (NW Spain). Environ. Geol. 52, 789–802. https://doi.org/10.1007/s00254-006-0516-6.

Luther, G., Giblin, A., Howarth, T., Ryans, R., 1982. Pyrite and oxidized iron mineral phases formed from pyrite oxidation. Geochimica et Cosmochimica 46 (12), 2665–2669. https://doi.org/10.1016/0016-7037(82)90385-4.

Luther III, G.W., 1991. Pyrite synthesis via polysulfide compounds. Geochim. Cosmochim. Acta 55 (10), 2839–2849. https://doi.org/10.1016/0016-7037(91)90449-F.

Margalef, R., 1952. Materiales para la hidrologia de isla de Menorca (Vol. XI). In: Publicaciones del Instituto de Biologia aplicada.

Mendelssohn, I.A., Kuhn, N.L., 2003. Sediment subsidy: effects on soil–plant responses in a rapidly submerging coastal salt marsh. Ecol. Eng. 21 (2), 115–128. https://doi.org/10.1016/j.ecoleng.2003.09.00.

Mikutta, R., Kleber, M., Kaiser, K., Jahn, R., 2005. Review: Organic matter removal from soils using hydrogen peroxide, sodium hypochlorite, and disodium peroxodisulfate. Soil Sci. Soc. Am. J. 69, 120–135. https://doi.org/10.2136/sssaj2005.0120.

Morse, J., 1991. Oxidation kinetics of sedimentary pyrite in seawater. Gvochimrca B Cosmochrmico Acta 55, 3665–3667. https://doi.org/10.1016/0016-7037(91)90064-C.

Morse, J.W., Mackenzie, F., 1990. Geochemistry of Sedimentary Carbonates (Vol. 48). Elsevier Science.

Odum, H., Odum, E., 1981. Hombre y Naturaleza : Bases Energéticas. Barcelona, Omega.

Oenema, O., 1990. Pyrite accumulation in salt marshes in the Eastern Scheldt, Southwest Netherlands. Biogeochemistry 9, 75–98. https://doi.org/10.1007/BF00002718.

Otero, X., Ferreira, T., Vidal-Torrado, P., Macías, F., 2006. Spatial variation in pore water geochemistry in a mangrove system (Paimatos island, Cananeia-Brazil). Appl. Geochem. 21 (12), 2171–2186. https://doi.org/10.1016/j.apgeochem.2006.07.012.
Otero, X., Ferreira, T., Huerta-Díaz, M., Partiti, C., Souza, J., Vidal-Torrado, P., Macías, F., 2009b. Geochemistry of iron and manganese in soils and sediments of a mangrove system, Island of Pai Matos (Cananeia- SP, Brazil). Geoderma 318–335.
Otero, X.L., 2000. Biogeoquímica de metales pesados en ambientes sedimentarios marinos. In: Universidad de Santiago de Compostela. Santiago de Compostela, Spain. PhD Thesis.
Otero, X.L., Macías, F., 2002. Variation with depth and season in metal sulfides in salt marsh soils. Biogeochemistry 61, 247–268. https://doi.org/10.1023/A:1020230213864.
Otero, X.L., Macías, F., 2003. Spatial variation in pyritization of trace metals in salt-marsh soils. Biogeochemistry 62, 59–86.
Otero, X.L., Macías, F., 2010. Biogeochemistry and Pedogenetic Process in Saltmarsh and Mangrove Systems. Nova Science Publishers Inc., New York, United States.
Otero, X.L., Vidal, P., Calvo, R., Macías, F., 2005. Trace elements in biodeposits and sediments from mussel culture in the ría de Arousa (Galica, NW Spain). Environ. Pollut. 119–134. https://doi.org/10.1016/j.envpol.2004.11.026.
Otero, X.L., Calvo de Anta, R., Macías, F., 2009a. Iron geochemistry under mussel rafts in the Galician ría system (Galicia-NW Spain). Estuarine, Coastal and Shelf 81 (1), 83–93. https://doi.org/10.1016/j.ecss.2008.10.006.
Otero, X.L., Huerta-Díaz, De La Peña, S., Ferreira, T., 2013. Sand as a relevant fraction in geochemical studies in intertidal environments. Environ Monit Assess 185 (10), 7945–7959. Retrieved from. https://www.ncbi.nlm.nih.gov/pubmed/23525774.
Otero, X.L., Lucheta, A., Ferreira, T., Huerta, M., Lambais, M., 2014. Archaeal diversity and the extent of iron and manganese pyritization in sediments from a tropical mangrove creek (Cardoso Island, Brazil). Estuar. Coast. Shelf Sci. 146, 1–13. https://doi.org/10.1016/j.ecss.2014.05.002.
Palomo, L., Meile, C., Joye, S., 2013. Drought impacts on biogeochemistry and microbial processes in salt marsh sediments: a flow-through reactor approach. Biogeochemistry 112, 389–407. https://doi.org/10.1007/s10533-012-9734-z.
Peiffer, S., Behrends, T., 2015. Pyrite formation and mineral transformation pathways upon sulfidation of ferric hydroxides depend on mineral type and sulfide concentration. Chem. Geol. 400, 44–55. https://doi.org/10.1016/j.chemgeo.2015.01.023.
Raiswell, R., Berner, R., 1985. Pyrite formation in euxinic and semi-euxinic sediments. American Journal of Science 285, 710–724. https://doi.org/10.2475/ajs.285.8.710.
Raiswell, R., Canfield, D., 1998. Sources of iron for pyrite formation in marine sediments. Am. J. Sci. 298 (3) https://doi.org/10.2475/ajs.298.3.219.
Ramírez-Pérez, A., de Blas, E., Otero, X.L., 2020. Iron pyritization in shallow methane fields in sediments of the Ría de Vigo (NW Iberian Peninsula). Estuar. Coast. Shelf Sci. 235, 106568. https://doi.org/10.1016/j.ecss.2019.10656.
Reimann, C., Filzmoser, P., Garrett, R., Dutter, R., 2008. Statistical Data Analysis Explained. John Wiley & Sons, Ltd, Chichester, UK.
Rickard, D., 1970. The Origin of Framboids. Lithos 3, 269–293. https://doi.org/10.1016/0024-4937(70)90079-4.
Rickard, D., 1975. Kinetics and mechanism of pyrite formation at low temperature. American Journal of Science 275, 636–652.
Rickard, D., 2012. Sulfidic Sediments and Sedimentary Rocks. Elsevier. https://doi.org/10.1016/B978-0-444-52989-3.00006-4.
Rickard, D., 2015. Pyrite: A Natural History of fool's Gold. Oxford University, New York.
Rickard, D., 2019a. How long does it take a pyrite framboid to form? Earth Planet. Sci. Lett. 513, 64–68. https://doi.org/10.1016/j.epsl.2019.02.019.
Rickard, D., 2019b. Sedimentary pyrite framboid size-frequency distributions: a meta-analysis. Palaeogeogr. Palaeoclimatol. Palaeoecol. 522, 62–75. https://doi.org/10.1016/j.palaeo.2019.03.010.
Roychoudhury, A., Kostka, J.E., Van Cappellen, P., 2003. Pyritization: a palaeoenvironmental and redox proxy reevaluated. Estuar. Coast. Shelf Sci. 57, 1183–1193. https://doi.org/10.1016/S0272-7714(03)00058-1.
Ruggiero, P., 2012. Is the intensifying wave climate of the US Pacific Northwest increasing flooding and erosion risk faster than sea-level rise. Journal of Waterway, Port, Coastal, Ocean Engineering 139 (2), 88–97. https://doi.org/10.1061/(asce)ww.1943-5460.0000172.
Sánchez, J., 1995. Caracterización florística y fitosociológica de las rías de Ortigueira y Ladrido (NW Península Ibérica) en relación con factores ambientales. PhD Thesis. Universidad de santaigo de Compostela. Santiago de Compostela, Spain.
Sánchez, J.M., Otero, X.L., Izco, J., Macías, F., 1997. Growth form and density of Spartina maritima (Curtis) Fernald in Northwest Spain. Wetlands 17 (3), 368–374.
Sánchez, J.M., Otero, X.L., Izco, J., 1998. Relationships between vegetation and environmental characteristics in a salt-marsh system on the coast of Northwest Spain. Plant Ecol. 136, 1–8. https://doi.org/10.1023/A:1009712629733.
Sánchez, M., Carballo, R., Ramos, V., Iglesias, G., 2014. Energy production from tidal currents in an estuary: a comparative study of floating and bottom-fixed turbines. Energy 77, 802–811. ISSN 0360-5442. https://doi.org/10.1016/j.energy.2014.09.053.
Schallreuter, R., 1984. Framboidal pyrite in deep sea sediments. Deep Sea Drilling 75, 875–891. Retrieved from. http://deepseadrilling.org/75/volume/dsdp75_24.pdf.
Scheffer, M., Carpenter, S., Foley, J., Walker, B., 2001. Catastrophic shifts in ecosystems. Nature 413, 591–596. https://doi.org/10.1038/35098000.
Schieber, J., Schimmelmann, A., 2007. High Resolution Study of Pyrite Framboid Distribution in Santa Barbara Basin Sediments and Implications for Water-Column Oxygenation. Pacific Climate Workshop, Pacific Grove, CA, pp. 31–32. Retrieved from. https://scholarworks.iu.edu/dspace/handle/2022/1819.
Souza, R.O., Vahl, L.C., Otero, X.L., 2009. Quimica dos Solos Alagados. In: Melo, V.F., Alleoni, L.R.F. (Eds.), Qu mica e Mineralogia do Solo vol. 2. SBCS, Viçosa, pp. 485–527.
Stone, M., Droppo, I., 1996. Distribution of lead, copper and zinc in size-fractionated river bed sediment in two agricultural catchments of southern Ontario, Canadá. Environ. Pollut. 93 (3), 353–362. https://doi.org/10.1016/S0269-7491(96)00038-3.
Taherkhani, M., Vitousek, P.L., Barnard, N.F., Anderson, T.R., Fletcher, C.H., 2020. Sea-level rise exponentially increases coastal flood frequency. Sci. Rep. 10 (1), 6466. https://doi.org/10.1038/s41598-020-62188-41.
Valiela, I., 2015. The Great Sippewissett salt marsh plots—some history, highlights, and contrails from a long-term study. Estuar. Coasts 38, 1099–1120. https://doi.org/10.1007/s12237-015-9976-9.
Valiela, I., Lloret, J., Bowyer, T., Miner, S., Remsen, D., Elmstrom, E., Cogswell, C., Thieler, E.R., 2018. Transient coastal landscapes: rising sea level threatens salt marshes. Science of Total Environment. https://doi.org/10.1016/j.scitotenv.2018.05.235.
Vallentyne, J.R., 1963. Isolation of pyrite spherules from recent sediments. Limnol. Oceanogr. 8 (1), 16–30. https://doi.org/10.4319/lo.1963.8.1.0016.
Wang, P., Huang, H., Wang, C., Feng, Z., Huang, Q., 2013. Pyrite morphology in the first member of the late cretaceous Qingshankou Formation, Songliao Basin, Northeast China. Palaeogeogr. Palaeoclimatol. Palaeoecol. 385 (385), 125–136. https://doi.org/10.1016/j.palaeo.2012.09.027.
Wiebe, W., Christian, R., Hansen, J., King, G., Skyring, B., Sherr, S., 1981. Anaerobic respiration and fermentation. In: The Ecology of a Salt Marsh, 38, pp. 137–159. https://doi.org/10.1007/978-1-4612-5893-3_7.
Wilkin, R., Barnes, H., 1997. Formation processes of framboidal pyrite. Geochim. Cosmochim. Acta 61 (2), 323–333. https://doi.org/10.1016/S0016-7037(96)00320-1.
Wilkin, R., Barnes, H., Brantley, S., 1996. The size distribution of framboidal pyrite in modern sediments: An indicator of redox conditions. Geochimica et Cosmochimica 60 (20), 3897–3912. https://doi.org/10.1016/0016-7037(96)00209-8.